The Influence of Modelling in Predictions of Vortex Interactions About a Generic Missile Airframe: RANS

Scott Shaw[1]

MBDA UK, Bristol, BS34 7QQ, United Kingdom

Anderson, Michael[2]

CORVID Technologies, Mooresville, NC 2811-8006, USA

Barakos, George[3] and Boychev, Kiril[4]

Glasgow University, Glasgow, G12 8QQ, United Kingdom

Dikbaş, Erdem[5]

Defense Industries Research and Development Institute (TÜBİTAK SAGE), Mamak, 06261, Ankara, Turkey

DeSpirito, James[6]

U.S. Army Combat Capabilities Development Center—Army Research Laboratory, USA

Loupy, Gaetan[7]

MBDA France, Paris, 92350, France

Schnepf, Christian[8]

German Aerospace Center (DLR), Göttingen, 37083, Germany

Tormalm, Magnus[9]

Swedish Defense Research Agency (FOI), SE-164 90, Stockholm, Sweden

---

[1] Corresponding Author, scott.shaw@mbda-systems.com, Senior-Principal Engineer, Aerodynamics, Propulsion and Lethality. AIAA Member.
[2] Computational Analyst, AIAA Member.
[3] Professor, Aerodynamics Department, AIAA Member.
[4] PhD Student, Aerodynamics Department, AIAA Member.
[5] Senior Research Engineer, Aerodynamics Division, AIAA Member.
[6] Aerospace Engineer, FCDD-RLW-WD, AIAA Associate Fellow
[7] Senior Engineer, Aerodynamics Department.
[8] Research Scientist, AIAA Member.
[9] Deputy Research Director, Department of Aerospace Engineering.

ABSTRACT

Within the framework of the NATO Science and Technology Organization Applied Vehicle Technology Task Group AVT316 calculations have been made of the supersonic flow around a slender body with wings and fins. In this paper a synthesis of the results obtained using the Reynolds Averaged Navier-Stokes equations are presented. The results show significant sensitivity to the choice of turbulence model. Whilst the gross features of the flow are similar, details of the development of the leeward wake are different. Simple linear eddy viscosity models predict vortices that rapidly decay, resulting in weak interactions with the downstream fins and relatively small rolling moments. This is attributed to an over production in turbulence quantities that results in excessive effective turbulent viscosity. Interventions that limit the production of turbulence, for example the SST limiter or curvature corrections, results in vortices that grow more slowly, changing the nature of the downstream interactions resulting in increased rolling moment. The use of more complex formulations, such as Reynolds stress models, that are inherently more capable for highly strained flows, further limits the rate of growth of the vortex cores leading to rolling moment predictions that are 2-3 times greater than those obtained with the simplest models.

I.   Nomenclature

C_l =   rolling moment coefficient, $C_l = L/qS$
d =   caliber
L =   rolling moment
M =   Mach number
q =   dynamic pressure, $q = \frac{\rho U^2}{2}$
Re_T =   turbulent Reynolds number, ratio of turbulent and molecular viscosity
S =   reference area, $S = \frac{\pi d^2}{4}$
U =   freestream velocity
x =   axial distance measured from the nose
y =   lateral distance measured from the missile center line
z =   vertical distance measured from the missile center line
δ =   boundary layer thickness
λ =   roll angle
ρ =   density
σ =   total incidence
Ω =   non-dimensional circulation, $\Omega = \Gamma/U\delta$
Γ =   circulation

II.   Introduction

In January 2018, the NATO Science and Technology Organization (STO) Applied Vehicle Technology (AVT) panel established a Task Group identified as AVT-316 (Vortex Interaction Effects Relevant to Military Air Vehicle Performance). The Task Group was split into two facets: an Aircraft Facet and a Missile Facet, each focusing on the vortex interactions associated with airframes of direct interest to NATO. The Missile Facet was established to (i) Assess the current capabilities of CFD to predict missile aerodynamic characteristics for flows containing multiple vortex interactions; (ii) Share and seek to learn from comparable experience of applying CFD to other classes of NATO vehicles (combat aircraft, in particular); and (iii) Consolidate lessons learned and any attendant future requirements [1]. This paper is one of a series being presented at this conference to provide a technical overview of the activities and accomplishments of the AVT-316 Missile Facet [2-11]. The work is still ongoing: a final output, constituting a more detailed and consolidated technical record, will be published by NATO STO towards the end of 2022 [68].

In high speed weapon aerodynamics, the generation of large scale vortical flow structures (vortices) within the flow can generally be related to the occurrence of two broad classes of flow separation that Smith [12] has

characterized as sharp edge separation and smooth wall separation. Vortices due to sharp edge separations include those from sharp leading edges, strakes, wing tips and discontinuous junction regions [13]. This class of vortices is directly associated with geometric features that fix the gross behavior of the flow separation. Vortices due to smooth-wall separations include those in the lee of blunt leading edge wings and slender bodies, faired junctions and as the result of secondary separation induced by interaction of primary vortices with the boundary layers of other aerodynamic surfaces. Smooth wall separation results from a failure of the boundary layer to negotiate an adverse pressure gradient and consequently the location and extent of the separation may change significantly with flow conditions. For the purposes of this introduction we limit our discussion to vortices associated with slender bodies (smooth wall separation) and wing tips (sharp edge separation), but most of our observations apply to vortex dominated flows more generally.

The flow around slender bodies at moderate to high incidence is dominated by the development of the leeside body wake resulting from smooth body crossflow separation. There have been a number of detailed experiments to understand the fundamental nature of such flows, see for example [14-22], and the basic phenomenology is well understood. There has also been a significant effort to model slender body flows using computational fluid dynamics (CFD). Of particular note are several collaborative initiatives sponsored by NATO [23], GARTEUR [24-27] and TTCP [28,29].

For laminar flows, the literature suggests that the steady Navier-Stokes equations are an adequate model to describe the behavior of the flow until the vortices become asymmetric in nature [24,25]. Comparisons with extensive experimental datasets show good correlation between the results of the numerical methods qualitatively, in terms of surface and volume flow topology, and quantitively using detailed surface and off surface flow measurements in both the boundary layer and vortex, and overall forces and moments. The situation for turbulent flows is much less satisfactory [25-29] with significant qualitative and quantitative differences being observed depending on the choice of mesh, numerical scheme and turbulence model. Khalid *et al* [23] provides a good review of the key turbulence modeling deficiencies most of which remain unaddressed in recent works.

Trailed vortices, such as those generated by sharp separation from a wing tip, share some similarities with slender body vortices. Like slender body vortices, they are compact flow features, but the absence of a feeding sheet means that they grow only through the action of viscous diffusion and so decay more slowly.

There are a number of theoretical results for laminar trailed vortices, see [30,31], that are reproduced adequately by integration of the steady Navier-Stokes equations. As with slender body vortices, the situation is less satisfactory for turbulent flows. In turbulent flows, the mean vortical flow acts to suppress the Reynolds shear stress, which in turn reduces the extraction of energy from the mean flow by the turbulence. This observation is important, because it suggests that the rate of growth of the vortex core through viscous diffusion should be controlled by molecular viscosity alone. Moreover, since the production rate is close to zero such quasi-laminar behavior should result in a decay of the turbulence contained in the vortex, see Zeman [32]. Experimental measurements appear to support this argument, see for example Zeman's analysis of the experimental data reported in [31].

For linear eddy viscosity turbulence models, without curvature or rotation correction, this quasi-laminar behavior of the vortex core flow is not observed. Indeed results from such models [32,33] produce an over-shoot in circulation consistent with the theoretical results of Govindaraju and Saffman [31] who assumed a turbulent core. For models that intrinsically model curvature effects (such as Reynolds stress transport models) or those models where such effects are addressed using a suitable palliative (for example a rotational or curvature correction) quasi-laminar behavior is observed, there is no over-shoot in circulation [32], and the effective turbulent viscosity rapidly diminishes [33].

Once created the dynamics of isolated vortices can be well described using inviscid theories, see for example Saffman [30]. However, in typical weapon aerodynamic applications the interaction of vortices with other flow features and downstream surfaces is important. In this paper the interaction of vortices with boundary layers and with each other in co-rotating and counter rotating pairs is of particular concern.

Due to their importance for flow management and control, vortex-boundary-layer interactions have been widely studied. A number of workers have made detailed measurements [34-39] that show that the circulation of the vortex, whether it is a single vortex or a co-rotating or counter-rotating pair, the orientation of the vortex with respect to the freestream and its position above the surface are all important.

For vortices that are well outside of the boundary layer, the interaction is weak and can be well predicted using inviscid theory [35] but as the distance from the wall is reduced, the interaction becomes stronger and changes both the boundary layer and the vortex characteristics. Harvey and Perry [36] have explored the case where the vortex, while remaining outside of the boundary layer, produces secondary flow within the boundary layer. In their explanation, they postulate that the primary vortex induces a crossflow on the surface and an associated suction peak, and for a strong enough vortex or a close enough approach to the wall, this adverse pressure gradient is sufficient to promote separation and an associated recirculation bubble. Progressing downstream this recirculation grows,

eventually separating from the surface to form a secondary vortex of opposite sense that is fed by a sheet of vorticity from the separation point. The subsequent dynamics of the vortex-vortex interaction are complicated, see below, but in the first instance the displacement effect of the re-circulation and the vortex will tend to push the primary vortex away from the surface, this is the so called vortex pair rebound. Subsequent experiments and theoretical analyses, see for example Peace [40], have confirmed this explanation. In the case of a slender body, the situation is further complicated by the presence of the primary vortex's feeding sheet, which acts to confine the motion of the secondary vortex.

The development of a single vortex and vortex pair embedded in the outer region of a turbulent boundary layer was investigated by Shabaka et al [37] and Mehta et al [38] respectively while Lin and his co-workers [39] have compared low profile vortex generators that create a primary vortex very close to the wall, with conventional vortex generators. The experiments suggest that the vortices induce vorticity of opposite sense and that this vorticity is convected away from the wall resulting in boundary layer fluid being entrained into the primary vortex. This mixing process can be exploited to delay boundary layer separation.

There is an extensive literature related to the application of computational fluid dynamics to these problems, see for example Spalart et al [41] for interactions where the vortex is outside of the boundary-layer, Allan et al [42] for interactions of a vortex in the outer part of the boundary layer and Wik [43] for interactions where the vortex is close to the surface. All of the studies illustrate the need for appropriate resolution and mesh quality and highlight weaknesses in common eddy viscosity turbulence models when dealing with highly strained flows.

While the underlying physical mechanisms are common to those observed for slender body vortex interactions it should be recognized that in most of the studies reviewed above, the non-dimensional circulation, $\Omega = \Gamma/U\delta$, is significantly smaller than those of slender bodies at high incidence. Cutler and Bradshaw [44, 45] have presented detailed experiments for weak (outside of the boundary layer) and strong (within the outer region of the boundary layer) interactions involving vortices with more representative circulation ($5 < \Omega < 50$). As expected the basic mechanisms are similar to those at low circulation, for example the importance of lateral divergence and convergence behavior on the downwards and upwards sides of the primary vortices and the tendency for fluid (and vorticity) to be lifted away from the surface by the primary vortex remain. However, there are some significant differences. In the case of weak vortices, the vortex must typically be embedded within the boundary layer to have any significant influence on the boundary layer itself, while for stronger vortices the vortex may exert significant influence over the boundary layer even when it is well outside. Indeed, the vortex pair rebound phenomenon detailed earlier may limit how close a strong vortex can come to the wall even when the vortex is generated close to the surface. Consequently, the lateral extent of the region of influence of the vortices is much greater for the strong interaction than that of the weak interaction.

For the case of vortex-vortex interaction, the interaction between pairs of counter-rotating vortices is of particular interest in the current work. The nature of this interaction depends on the relative strength, size and distance between the cores. Meunier and his co-workers [46] provide a comprehensive description of the physics of vortex merging. For well separated corotating vortices, the individual cores remain coherent and the vortices rotate around a common point at a rate depending on the strength of the vortices and their separation distance. This process leads to braiding. As the vortices age, their cores spread by viscous diffusion, the ratio of core diameter to separation distance increases and the vortices begin to merge. The merging process is characterized by two key stages; firstly convective merging in which the vortex undergoes rapid deformation, filaments or arms of ejected vorticity are created that rotate around the cores and there is a significant reduction in separation distance resulting in two close but distinct vorticity maxima. The structure then undergoes diffusive merging, and the vortex cores merge resulting in a single axisymmetric vortex.

This paper presents the results of computations performed using several turbulence models for the OTC1 test case performed in the frame of the NATO sponsored AVT316 activity. All of the calculations have been performed for the nominal flow condition, a Mach number M=1.4, a total incidence of $\sigma = 15°$, a roll angle of $\lambda = -2.5°$ and a Reynolds number of 4.9 million based upon the diameter of the missile body.

The paper is structured as follows. In the next section we briefly consider whether the Navier-Stokes equations are a suitable basis for studying the OTC1 test case. Having qualified the underlying physical model we then consider the performance of linear eddy viscosity turbulence models based upon the Spalart-Allmaras [47] and Menter k-ω SST [48] turbulence models. The performance of non-linear turbulence closures and models that resolve the turbulent shear stresses directly is then considered. In the final section, conclusions and recommendations are made.

4

III.   Conceptual Modeling

All of the results presented in this paper are based upon the numerical solution of the Navier-Stokes equations. A detailed derivation of this system of equations is beyond the scope of this paper, but can be found in standard texts [49,50].

In formulating the Navier-Stokes equations we make a number of significant assumptions. These include that the fluid is a continuum (allowing us to bring the tools of Newtonian mechanics to bear), that it is an ideal gas (equation of state), that it is a Newtonian fluid (a simple constitutive relationship between stress and strain) and so on. In addition, we introduce a number of sub-models, for example Sutherland's law (an empirical relationship between the coefficient of molecular viscosity to temperature), in order to close the resulting system of equations.

For the flows that are of interest in the present study, all such modeling assumptions are reasonable and the conditions of interest lie within the calibrated range of the sub-models. For our purposes the Navier-Stokes equations can be qualified as a good model.

The computational cost of resolving the length and time scales associated with flows at typical application Reynolds numbers, $O(10^6)$ based upon the missile diameter, are such that numerical resolution of the Navier-Stokes equations, known as Direct Numerical Simulation (DNS), is prohibitively expensive. Instead additional simplifying assumptions are made with respect to how turbulence is represented.

There are two natural approaches to dealing with turbulence; filtering and averaging. Filtering the Navier–Stokes equations is the basis of Large Eddy Simulations (LES). In this approach the dynamics of the turbulence is filtered based upon the size of turbulent eddies. Only the largest eddies (associated with the largest length and time scales) are directly resolved while the effects of smaller eddies are modeled using a sub-grid-scale (SGS) model. While this approach reduces the cost of calculations considerably, they remain sufficiently high to prevent widespread adoption of LES within industry. The cost of evaluating the model can be reduced further by averaging turbulent velocity fluctuations in time. For compressible flows such averaging can be achieved using a direct (kinematic) ensemble average or density weighted (dynamic) ensemble average to obtain the Reynolds-averaged and Favre-averaged Navier-Stokes equations respectively [50]. Both Reynolds- and Favre-averaged Navier-Stokes equations require a model of turbulence that relates averages of the turbulent fluctuations to mean flow quantities. A third approach, Detached Eddy Simulation (DES), can be obtained by applying filtering and averaging in different regions of the flow [51].

In this paper we present results that have been obtained using a turbulence model approach. Several different turbulence closures have been investigated. In a companion paper [6] the results of scale-resolving approaches, such as DES, are reported.

IV.   Turbulence Modeling

For compressible flows the following generic model equation is suggested [50],

$$\bar{\rho}\frac{D\varphi}{Dt} = S_P + D - S_D \qquad (1)$$

in which the dependent variable φ represents a modeled turbulence quantity, for example the turbulent kinetic energy k. The terms on the right-hand-side of Equation 1 represent the production (S_P), molecular diffusion and turbulent transport (D), and dissipation (S_D) of the modeled quantity. Using the continuity equation this equation can be cast in the familiar conservative form,

$$\frac{\partial\bar{\rho}\varphi}{\partial t} + \frac{\partial}{\partial x_j}\bar{\rho}\left(\varphi\tilde{u}_j - (\mu + \mu_t)\frac{\partial\varphi}{\partial x_j}\right) = S_P + \bar{D} - S_D \qquad (2)$$

in writing Equation 2 it is convenient to split the molecular and turbulent transport into two parts such that $D = \frac{\partial}{\partial x_j}\left(\bar{\rho}(\mu + \mu_t)\frac{\partial\varphi}{\partial x_j}\right) + \bar{D}$.

Several turbulence models have been investigated in the current work. For the purposes of our discussion we will consider the models in four broad groups: (i) linear eddy viscosity models that employ the Boussinesq hypothesis, (ii) models with curvature and rotational correction, (iii) models that employ a non-linear constitutive relationship, and (iv) models that directly resolve the Reynolds stresses.

The paper makes use of results generated by the authors, each of whom has used their own mesh generator, solver and best practice. Table 1. provides a summary of some details of the software used by the authors to perform the

calculations. In the paper we will draw upon individual results to support our observations on the performance of the models and some theoretical arguments. The authors caution readers against using the results to make comparisons and judgements about the relative performance of individual codes.

Partner	Mesh Generator	Mesh Type	Solver	Discretization Scheme
ARL	Capstone	Unstructured	CFD++	Cell-Centered (HLLC)
ARL	Capstone	Unstructured	Kestrel	Cell-Centered (HLLE+)
Corvid Technologies	Pointwise	Unstructured	Raven	Cell-Centered (LDFSS(3))
DLR	Centaur	Unstructured	Tau	Cell-Vertex (Central Difference)
				Cell-Vertex (AUSMDV)
FOI	ANSYS ICEM CFD TriTet, Pointwise	Unstructured	M-Edge	Cell-Vertex (Central Difference)
Glasgow University	ANSYS ICEM CFD Hexa	Structured - Overset	HMB3	Cell-Centered (Osher)
MBDA-France	ANSA	Unstructured	FLUSEPA	Cell-Centered
MBDA-UK	Solar	Unstructured	Tau	Cell-Vertex (Central Difference)
				Cell-Vertex (AUSMDV)
MBDA-UK	Pointwise	Structured	Tau	Cell-Vertex (Central Difference)
				Cell-Vertex (AUSMDV)
Turbitak-Sage	ANSYS ICEM CFD TGRID	Unstructured	Fluent	Cell-Centered

Table 1   Details of the software used by the partners.

A. Linear Eddy Viscosity Models

Linear eddy viscosity turbulence models employ the concept of an effective turbulent (eddy) viscosity. By analogy with molecular viscosity, Boussinesq hypothesized that the additional turbulent stresses that appear in the RANS equations could be related to the mean rate of strain using a simple linear constitutive relationship. The coefficient of proportionality in that relationship is an effective turbulent viscosity which, unlike the molecular viscosity, is a property of the flow. This hypothesis has proven extraordinarily useful in modeling turbulent flows and is the basis of many simple engineering models such as those due to Spalart and Allmaras [47] and Menter [48].

1. Spalart-Allmaras Model

The standard Spalart-Allmaras one-equation eddy viscosity model [47] was originally introduced to provide a general treatment of turbulence in wall bounded flows and free shear-layers. Since then it has been widely adopted due to the ease with which it can be implemented and it's relative accuracy in comparison to its peers. The model solves for a quantity related to the eddy viscosity, $\hat{v}$, using,

$$\frac{\partial \hat{v}}{\partial t} + u_i \frac{\partial \hat{v}}{\partial x_j} = S_P + D - S_D \qquad (3)$$

with the production, dissipation and diffusion terms,

$$S_P = c_{b1}(1 - f_{t2})\hat{S}\hat{v} \qquad (4)$$

6

$$S_D = \left(c_{w1}f_w - \frac{c_{b1}}{\kappa^2}f_{t2}\right)\left(\frac{\hat{v}}{d}\right)^2 \tag{5}$$

$$D = \frac{1}{\sigma}\left(\frac{\partial}{\partial x_j}\left((\hat{v} + \hat{v}_t)\frac{\partial\hat{v}}{\partial x_j}\right) + c_{b2}\frac{\partial\hat{v}}{\partial x_i}\frac{\partial\hat{v}}{\partial x_i}\right) \tag{6}$$

The turbulent viscosity can be computed from,

$$\mu_t = \bar{\rho}\hat{v}f_{v1} \tag{7}$$

Details of the model coefficients and auxiliary functions can be found in [47]. The trip term f_{t2}, which is related to the modeling of transition from laminar to turbulent flow, was not used in any of the computations reported in this work. Using the taxonomy suggested by [52], results for this model will be referred to using the designation SA-noft2.

More recently Allmaras, Johnson and Spalart [53] reformulated the model to address issues with under-resolved meshes and non-physical transient states. This negative formulation of the Spalart-Allmaras model is identical to the original model when the eddy viscosity is greater than or equal to zero. But when $\hat{v}$ is negative the right hand side terms are altered, see [53] for the full formulation. Results from this model will be referred to using the designation SA-neg.

Fig. 1 shows contours of total pressure ratio obtained at various locations along the axis of the OTC1 missile at the nominal flow condition by MBDA UK using the SA-neg turbulence model. The flow development over the forebody closely matches that expected for slender bodies. Despite a significant thickening of the leeside boundary layer, there is little evidence of crossflow separation over the nose (x/D > -2.0) and it is not until x/D = -3.0, a caliber aft of the nose body apex, that crossflow separation first becomes evident. The separated shear layers roll up to form a pair of coherent counter rotating vortices in the leeside wake of the body. The vortex cores grow in size and the mutual interaction between the vortices and body causes them to be pushed away from the feeding sheet. The resultant stretching produces a non-circular core. The effects of the slight flow asymmetry produced by the roll angle are clearly visible with the starboard side separation occurring slightly later than on the port side. This difference in separation location is evident in the relative position of the vortex cores. There is some evidence of secondary separation below the primary vortices.

The immediate effect of the wings is to detach the forebody vortices from their feeding sheets (see for example x/D = -8.1) resulting in an outwards movement of the vortex core. The forebody vortices continue to grow becoming more circular in shape. At the same time additional vortices begin to form along the tips of the wings. The development of the windward and leeward tip vortices is very different. On the leeward side the behavior of the tip vortex is dominated by its interaction with the forebody vortex. The vortices are co-rotating and initially well separated, the individual cores remain coherent and rotate about one another. As the vortices age further, their cores spread by viscous diffusion, the ratio of core diameter to separation distance increases and the vortices begin to merge. This process is relatively rapid and results in forebody and tip vortices merging into a single vortex, see for example x/D = -11.0. Once the merging of the forebody and wing tip vortices on the leeward-side has completed the vortex grows rapidly and develops an elliptical shape. On the windward side the vortex development is similar to that observed for low aspect ratio wings, and once it has formed the vortex grows rapidly and develops an elliptical shape.

Downstream of the wings there are two features of note. Firstly, there is evidence of a strong interaction between the leeward and windward vortices. It appears that the vortices rotate around one another, although the structures are indistinct. In addition, the wake structure that develops behind the wings (x/D = -17.1) interacts with the free vortices and is entrained into the vortical flow (x/D = -19.0). By the time the flow reaches the missile fins the wing wake structure is no longer distinct. The interaction of the remnants of the forebody vortex with fin 4 appears strong with the wing tip appearing to pass through the core (x/D = -21.9, x/D = -22.1).

Our quantitative description of the vortex evolution relies on two basic scalar descriptors; the location of the vortex core (lateral location y/D, vertical location z/D) and the local extrema in streamwise vorticity ((ω_x D)/U) at the vortex core. These descriptors provide information about the location and concentration of vorticity in the core. The development of total pressure at the core, which can be inferred from the peak vorticity, is also shown for completeness. Other common descriptors, such as circulation (a measure of vortex strength) and core size (a further measure of vortex concentration) were not evaluated due to the difficulty of isolating contributions to individual vortices in the interactions downstream of the wing leading edge.

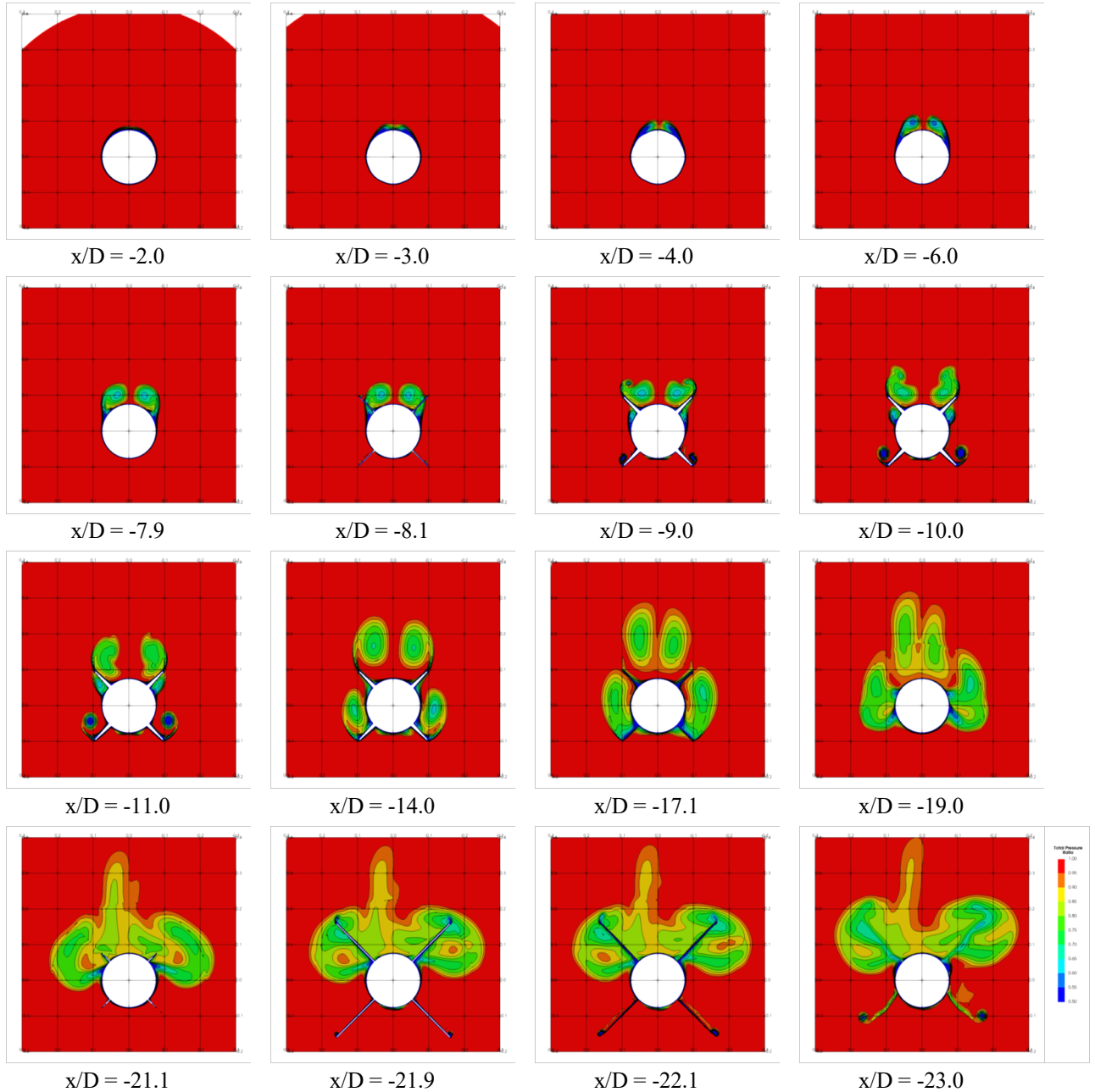| x/D = -2.0 | x/D = -3.0 | x/D = -4.0 | x/D = -6.0 |
x/D = -7.9	x/D = -8.1	x/D = -9.0	x/D = -10.0
x/D = -11.0	x/D = -14.0	x/D = -17.1	x/D = -19.0
x/D = -21.1	x/D = -21.9	x/D = -22.1	x/D = -23.0

Fig. 1 Evolution of the flow around the OTC1 missile at the nominal flow condition, contours of normalized total pressure (SA-neg model, MBDA-UK structured mesh).

Fig. 2 and Fig. 3 show computed vortex descriptors obtained by Corvid Technologies using the SA-noft2 model for the windward and leeward side respectively. The data support the qualitative description provided above. On the leeward side the body vortex first becomes evident at around x/D = -3.0. This location is consistent with the empirical model of Mendenhall and Nielsen [54]. Peak vorticity is initially high and diminishes gradually with distance downstream as the vortex core grows in size. The vertical and lateral locations of the vortex core immediately ahead of the wing leading edge are also consistent with the model suggested in [54]. The interaction of the vortex with the wing leading edges results in a significant lateral displacement of the center , while at x/D = -10.0 there is a further peak in vorticity as the forebody vortex merges with the wing tip vortex. On the windward side, the development of peak vorticity suggests that the core of the wing tip vortex grows rapidly. The peak vorticity has diminished by around 90% of its initial value by the wing trailing edge.
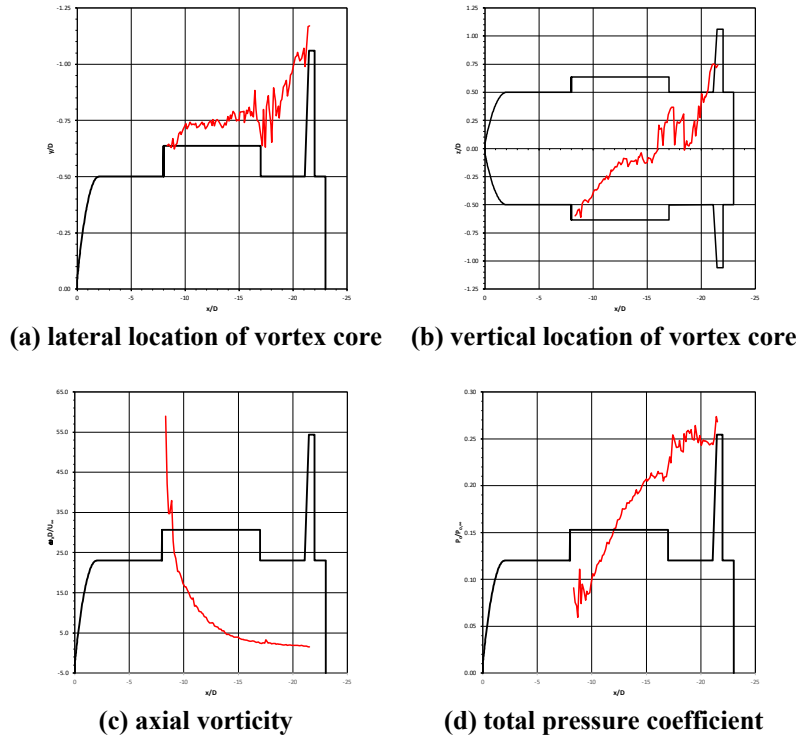
(a) lateral location of vortex core   (b) vertical location of vortex core

(c) axial vorticity   (d) total pressure coefficient

Fig. 2 Leeside vortex descriptors (SA-noft2 model, Corvid Technologies, unstructured mesh).

(a) lateral location of vortex core   (b) vertical location of vortex core

(c) axial vorticity   (d) total pressure coefficient
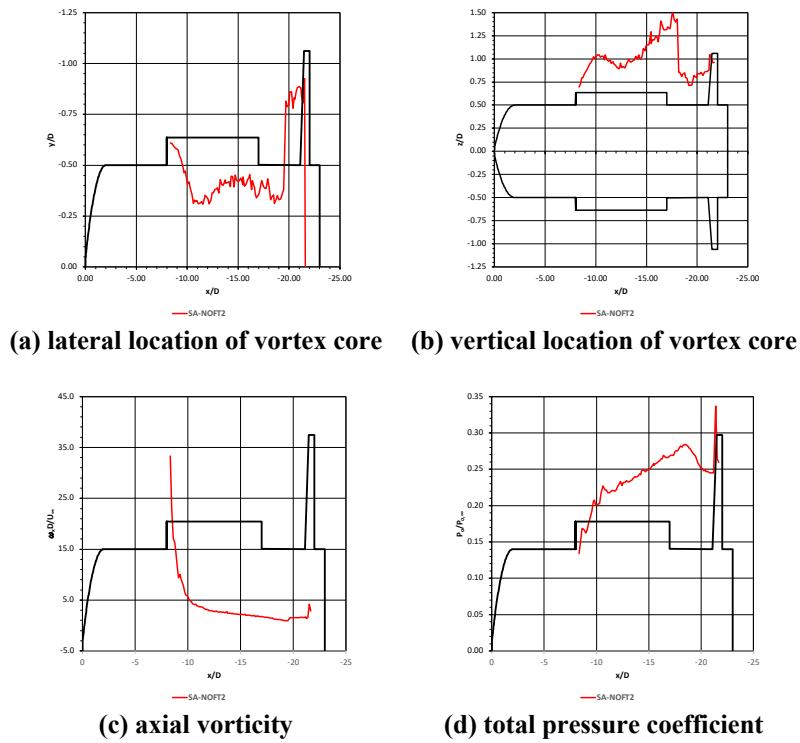
Fig. 3 Windward vortex descriptors (SA-noft2 model, Corvid Technologies, unstructured mesh).

In their original presentation of the model, Spalart and Allmaras [47] note that 'in the flows of interest to us, turbulence is found only where vorticity is present, with both emanating from solid boundaries'. As a consequence they employ magnitude of vorticity as a scalar measure of the deformation tensor and restrict the calibration of the model to simple shear layers. In order to understand the implications of this for flows involving free vortices we consider the condition for turbulent equilibrium. For turbulent equilibrium the source terms on the right-hand side of Equation 1 must balance. For the SA-noft2 and SA-neg models this requires that,

$$\hat{v} = \frac{c_{b1}\kappa^2}{\kappa^2 c_{w1}f_w - c_{b1}f_{v2}} S d^2 \qquad (8)$$

we observe that when the production and dissipation terms are in balance the turbulent viscosity is proportional to the product of vorticity magnitude and the square of the distance from the surface. For simple shear layers this results in the expected behavior, a turbulent viscosity that is zero, but in the presence of coherent structures outside of the boundary layer where the magnitude of vorticity is not negligible we expect that the value of this product will be high. This expectation is confirmed by Fig. 4 which shows contours of turbulent Reynolds number (the ratio of turbulent and molecular viscosity) at stations immediately ahead of the wing leading and trailing edges and Fig. 5 which shows the development of the turbulent viscosity ratio along the core of the vortex. Although there are no corresponding experimental measurements this behavior, $Re_T > 5000$, is thought to be non-physical.

<div style="text-align:center">

(a) x/D = -7.9   **(b) x/D = -16.9**
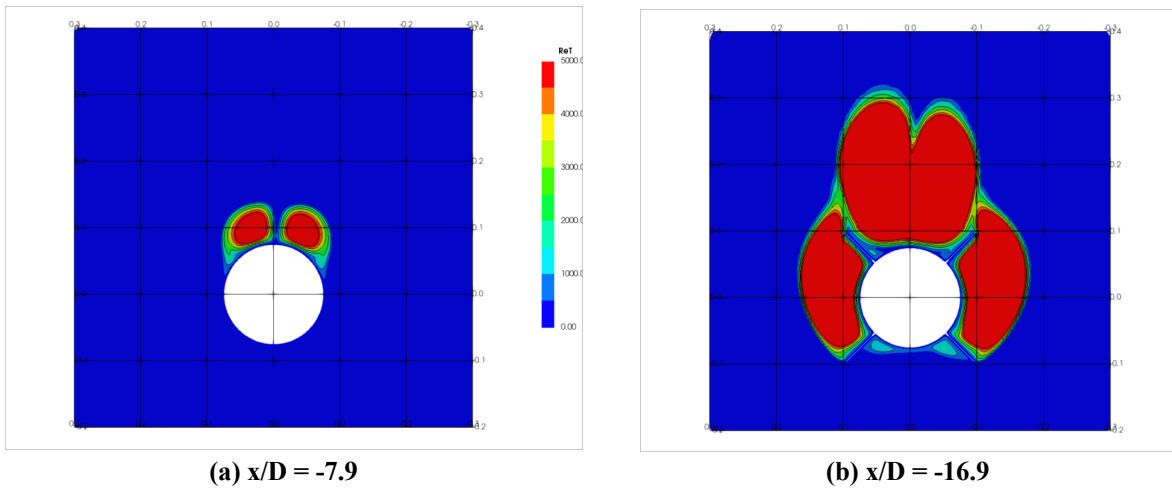
Fig. 4 Contours of turbulent Reynolds number (SA-neg model, MBDA UK, structured mesh).

</div>

<div style="text-align:center">

(a) windward side   **(b) leeward side**
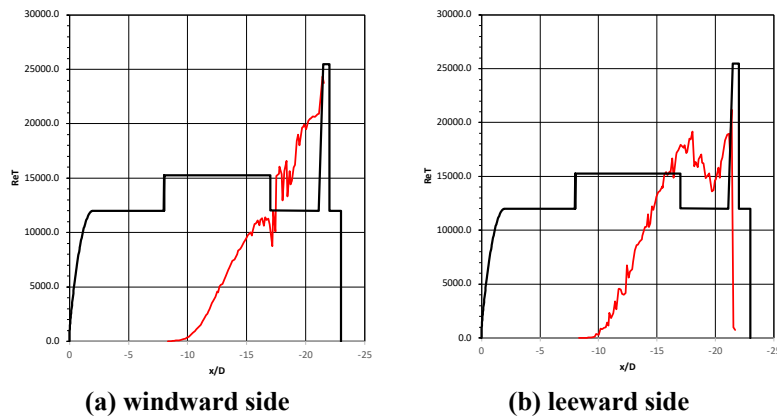
Fig. 5 Evolution of turbulent Reynolds number (SA-noft2 model, Corvid Technologies, unstructured mesh).

</div>

Fig. 6 presents computed rolling moment results obtained using the SA-noft2 model for various flow solvers on a common unstructured mesh [3] (the mesh has around 84 million nodes and 240 million elements). As no systematic mesh convergence exercise has been perfromed, it is difficult to draw any firm conclusion beyond noting the significant variation in the computed data. It is suggested that this is largely due to the different discretization schemes employed by the different solvers. There is some weak evidence for this suggestion in the Tau results, where computations performed of the rolling moment based on solutions obtained using both central difference and upwind discretization schemes show a significant (approximately 15%) difference.
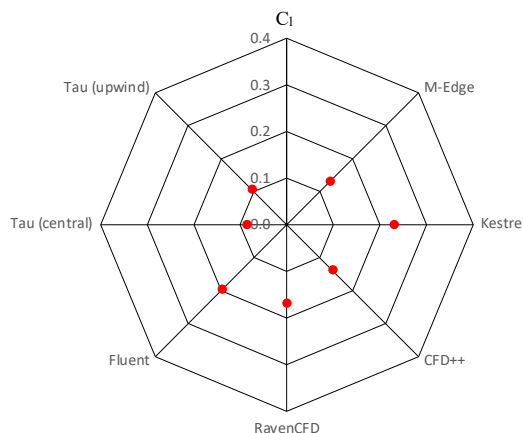
Fig. 6 Comparison of computed rolling moment coefficient (C_l) (SA-noft2 model, common unstructured mesh).

Several of the authors initially used a first-order discretization of the convective terms in the model equations for turbulence. This is a relatively common approach and has been justified, see for example Menter [48], on the basis that discretization errors in the transport terms of the turbulence model equations are not leading order terms in the overall discretization error. However, as shown in the results provided by ARL and DLR, Fig. 7, there does appear to be significant differences between the use of a first-order and second-order approximation of the turbulence equations for this case. Indeed, for some solvers and grids moving from a first to second-order scheme results in a halving of the magnitude of the rolling moment coefficient. This results seems counter-intuitive, we typically associate increased dissipation in the numerical scheme with a weaker, more diffuse vortex. However, in this case it is quantities associated with the turbulence that are more rapidly dissipated, rather than mean flow quantities such as pressure and velocity. This leads to reduced effective turbulent viscosity and consequently a stronger vortex. This can be seen in Fig. 8 and Fig. 9 which compare contours of turbulent Reynolds number and total pressure coefficient ratio computed using a first- and second-order discretization scheme at x/D = -19.0 and x/D = -21.5.
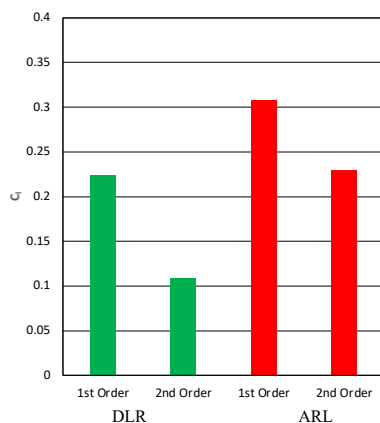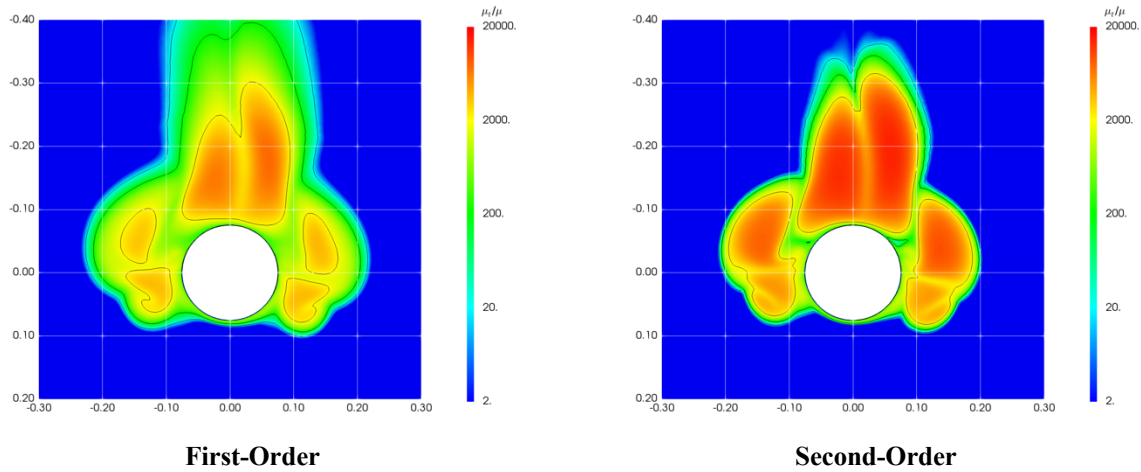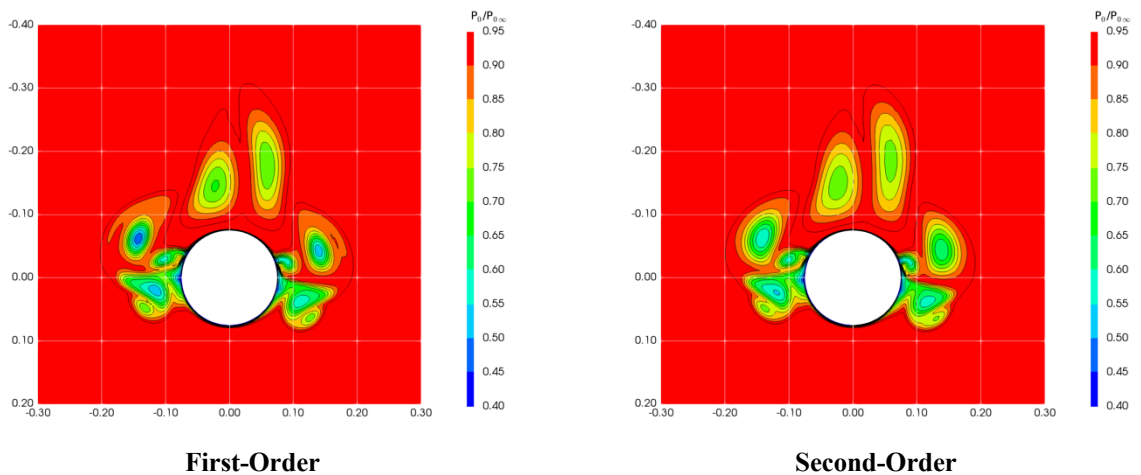

Fig. 7 Comparison of computed rolling moment coefficient (C_l) obtained using first- and second-order discretization of the SA-noft2 turbulence model equation (unstructured mesh).

11

First-Order   **Second-Order**

(a) Turbulent Reynolds number (μ_t/μ)

First-Order   **Second-Order**
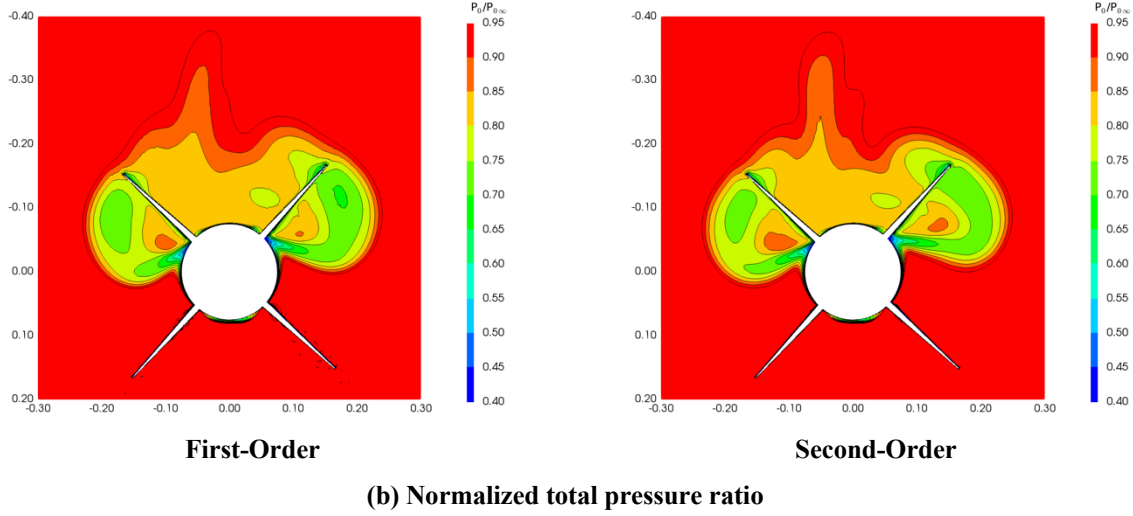
(b) Normalized total pressure ratio

Fig. 8 Comparison of computed flow field characteristics x/D=-19.0 using first- and second-order discretization of the turbulence model equation (SA-noft2 model, ARL, unstructured mesh).

First-Order   **Second-Order**

(a) Turbulent Reynolds number (μ_t/μ)

First-Order   **Second-Order**

(b) Normalized total pressure ratio
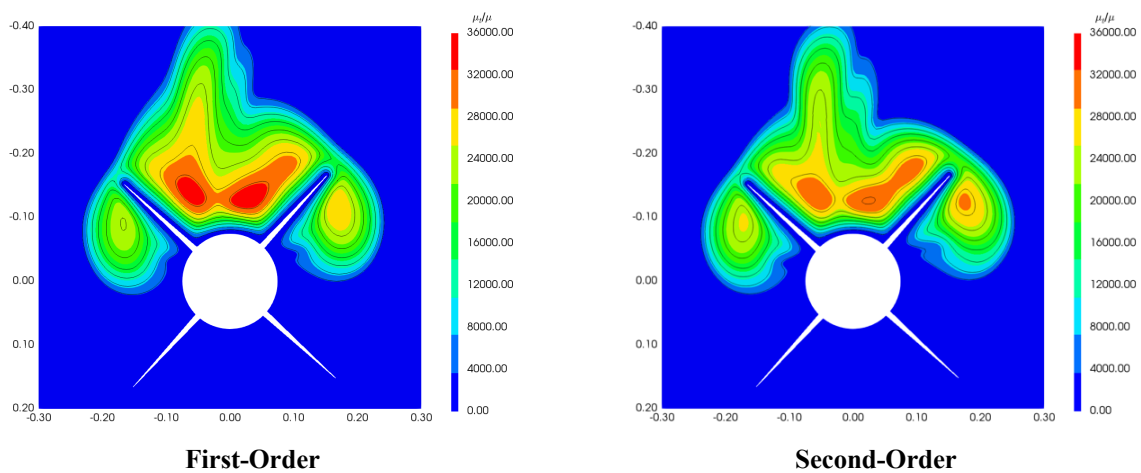
Fig. 9 Comparison of computed flow field characteristics x/D = -21.5 using first- and second-order discretization of the turbulence model equation (SA-noft2 model, DLR, unstructured mesh).

2. k-ω SST Model (SST)

Menter [48] conceived his k-ω SST Model in order to address the need for the accurate prediction of aeronautics flows with strong adverse pressure gradients and separation. At the heart of the model is the use of a zonal approach, the so called baseline (BSL) model, that relies on Wilcox's k-ω turbulence model [55] to compute the near wall flow and a k-ε model [56] in the outer part of the boundary layer. Building on the observation that the ratio of production to dissipation was significantly above one in the presence of an adverse pressure gradient Menter used Bradhsaw's assumption to limit the development of the principal shear stress (Equation (14) below).

In conservation form, the standard model equations given in [48] are,

$$\frac{\partial(\rho k)}{\partial t} + \frac{\partial(\rho u_i k)}{\partial x_j} = P + \frac{\partial}{\partial x_j}\left(\left(\mu + \sigma_k \mu_t\right)\frac{\partial k}{\partial x_j}\right) - \beta^* \rho \omega k \tag{9}$$

$$\frac{\partial(\rho \omega)}{\partial t} + \frac{\partial(\rho u_i \omega)}{\partial x_j} = \frac{\gamma}{\nu_t}P + \frac{\partial}{\partial x_j}\left(\left(\mu + \sigma_\omega \mu_t\right)\frac{\partial \omega}{\partial x_j}\right) - \beta \rho \omega^2 + 2(1 - F_1)\frac{\rho \sigma_{\omega 2}}{\omega}\frac{\partial k}{\partial x_j}\frac{\partial \omega}{\partial x_j} \tag{10}$$

with the production, dissipation and diffusion terms,

$$P = \tau_{ij}\frac{\partial u_i}{\partial x_j} \tag{11}$$

$$\tau_{ij} = \mu_t\left(2S_{ij} - \frac{2}{3}\frac{\partial u_k}{\partial x_k}\delta_{ij}\right) - \frac{2}{3}\rho k \delta_{ij} \tag{12}$$

$$S_{ij} = \frac{1}{2}\left(\frac{\partial u_i}{\partial x_j} + \frac{\partial u_j}{\partial x_i}\right) \tag{13}$$

The turbulent viscosity is obtained from,

$$\mu_t = \frac{\rho a_1 k}{max(a_1 \omega, \Omega F_2)} \tag{14}$$

Details of the remaining constants can be found in [48]. We shall refer to this model using the designation SST in the remainder of this work. A key feature of many implementations of the SST model is the use of limiters.

13

In his original presentation of the model Menter introduced a production limiter [57],

$$P = min(P, 20\beta^*\rho\omega k) \qquad (15)$$

to overcome numerical problems associated with the production term for eddy viscosity which can, when ω is close to zero, tend to infinity for small disturbances in the rate of strain tensor. The modification also eliminates unphysical behavior in stagnation regions. More recently Menter et al [58] have suggested a limiting factor of 10 be used instead of 20, based upon their experience applying the model to a wide range of flows. They note that for simple boundary layers the ratio of production to dissipation rarely exceeds 2. Some implementations also impose a lower bound on the production term such that,

$$P = max(0, min(P, 20\beta^*\rho\omega k)) \qquad (15a)$$

which ensures that the production term is always positive.
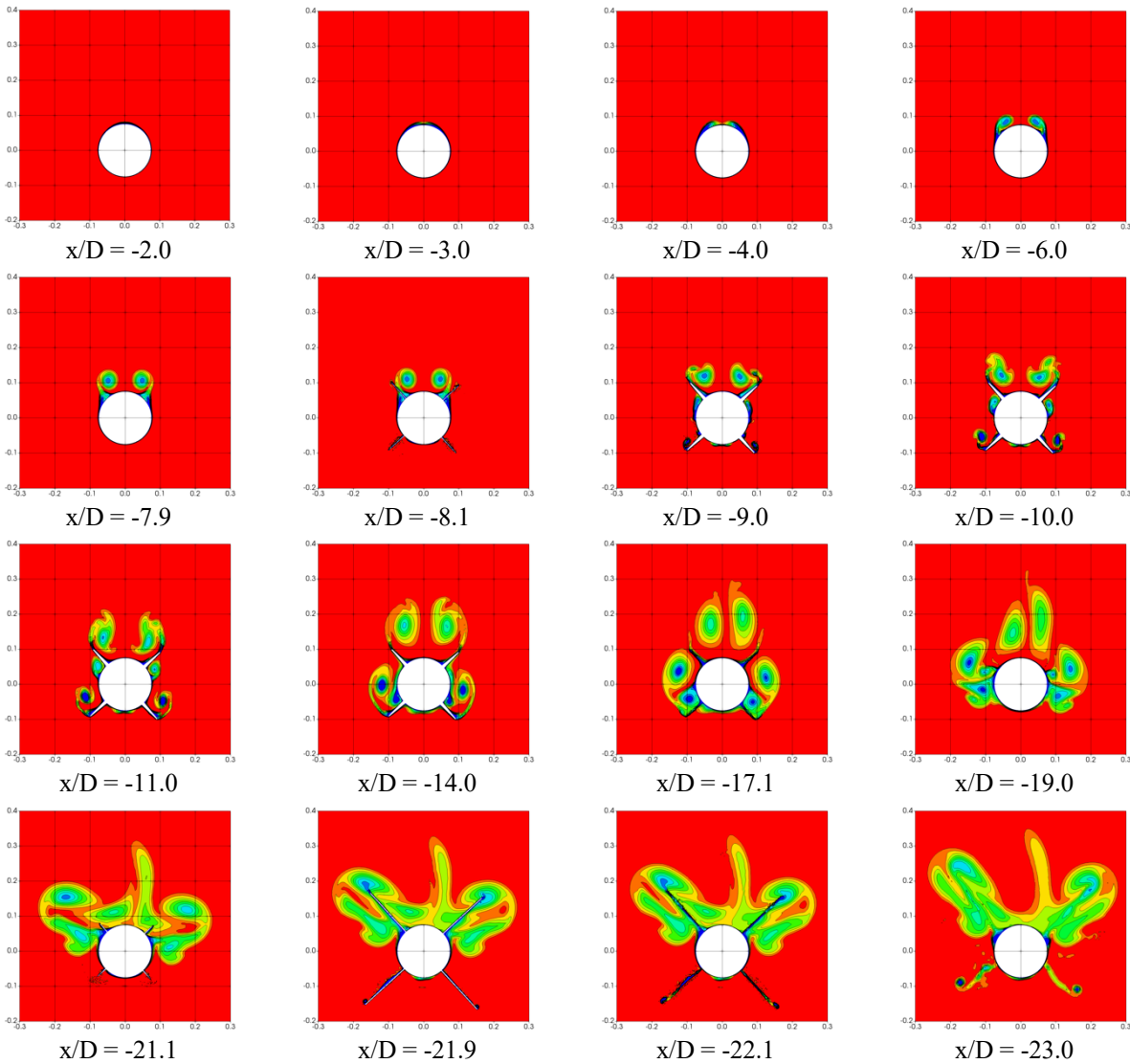
Fig. 10 Evolution of the flow around the OTC1 missile at the nominal flow condition (SST model, DLR, unstructured mesh.

14

Fig. 10 shows contours of total pressure ratio obtained using the SST model at various locations along the axis of the OTC1 missile at the nominal flow condition, whilst Fig. 11 and Fig. 12. show the corresponding vortex descriptors for the leeward and windward flows respectively. The development of the flow closely follows that observed for the SA-neg turbulence model, see the discussion of Fig. 1. As with the results generated using the SA-noft2 and SA-neg models, it appears that SST models result in erroneous levels of turbulence in the vortices. This can be seen clearly in Fig. 13, which shows contours of turbulent kinetic energy at x/D = -23.5 computed by ARL and FOI and Fig. 14, which shows contours of turbulent Reynolds number at x/D = -21.5.

The flow development seen in the solution of the SST model is broadly similar to that seen for the SA-neg model. The main differences lie in the computed vortex characteristics. On the windward side of the body, the vortex trajectory compares very well with that seen in the results from the SA-noft2 model. The peak vorticity also compares favorably initially, but decays more gradually than in the SA-noft2 calculations, resulting in a much stronger vortex over the wing, aft body and fins. For the leeward side vortex system, the vertical location of the vortex core is similar to that seen using the SA-noft2 model, but the lateral location is more outboard. The vortex is initially much stronger than seen using the SA-noft2 model, but decays more rapidly. In spite of the more rapid decay the vortex predicted using the SST model is much stronger than that obtained using the SA-noft2 model over the full length of the missile.

The rolling moment coefficient obtained using the SST model is compared with that found using the SA-noft2 model in Fig. 15. We see that for all authors a much larger rolling moment coefficient, in some cases more than double, was obtained with the SST model.
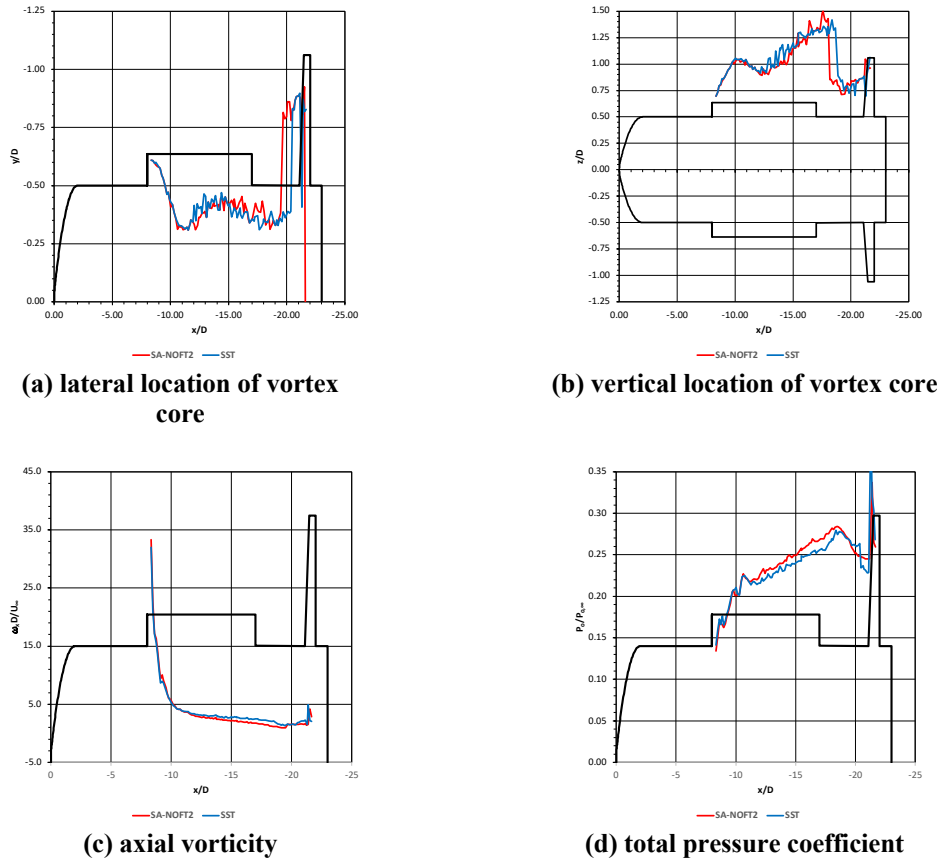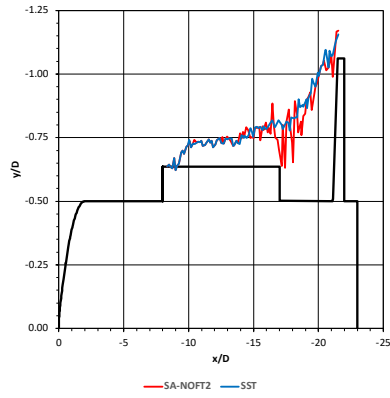

(a) lateral location of vortex core

(b) vertical location of vortex core

(c) axial vorticity

(d) total pressure coefficient

Fig. 11 Leeside vortex descriptors (SST model, Corvid Technologies, unstructured mesh).

The spurious over production of turbulence in the vortex core is perhaps unexpected. One might anticipate that the Bradshaw limiter, Equation 14, would be active and act to reduce the production term. However, the detailed formulation of the blending function F_2 is important. The blending function is designed such that $F_2 = 1$ within the boundary layer and $F_2 = 0$ elsewhere. Thus Equation 14 is limited to,
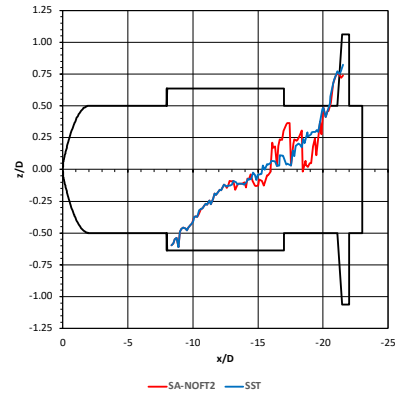
$$\mu_t = \frac{\rho a_1 k}{\Omega} \qquad (14a)$$

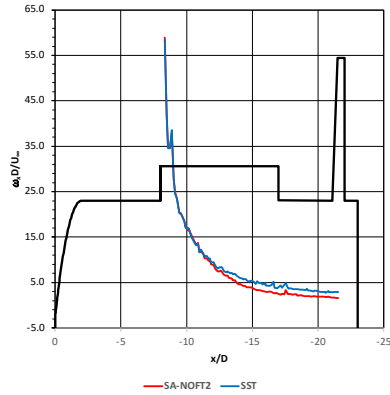in the boundary layer but is intended to be unlimited elsewhere, that is,
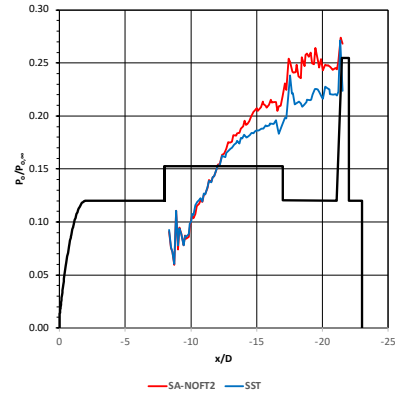
$$\mu_t = \frac{\rho k}{\omega} \qquad\qquad (14b)$$

(a) lateral location of vortex core
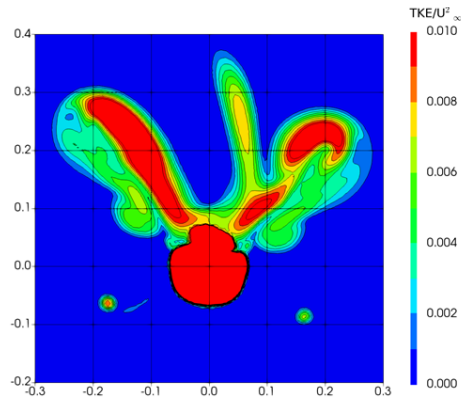

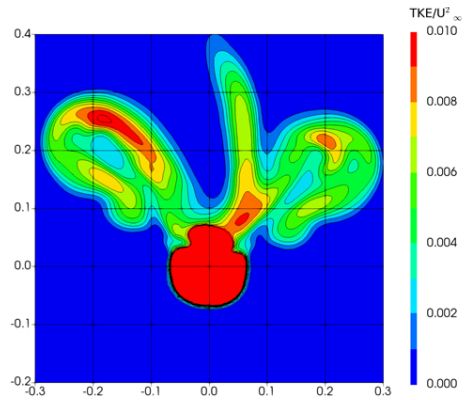**(b) vertical location of vortex core**

(c) axial vorticity

(d) total pressure coefficient

Fig. 12 Windward vortex descriptors (SST model, Corvid Technologies, unstructured mesh).

(a) ARL

(b) FOI

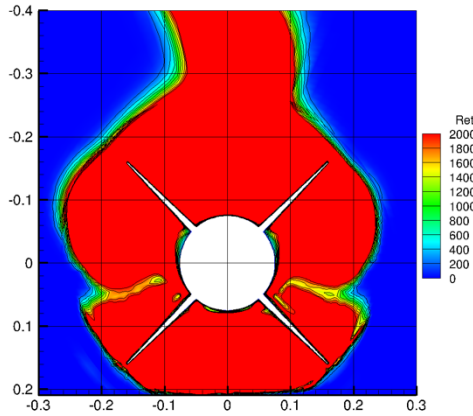**Fig. 13 Contours of computed turbulent kinetic energy x/D = -23 (SST model, DLR shared mesh).**

16

Fig. 14 Contours of turbulent Reynolds number, x/D = -21.5 (SST Model, Glasgow University, structured mesh).
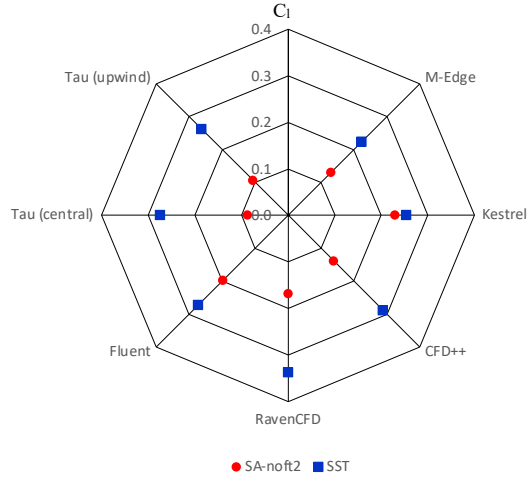

Fig. 15 Comparison of rolling moment coefficients obtained using SST and SA-noft2 models (unstructured mesh).

In order to demonstrate the effects of the production term limiter, Equation 15, on the predicted rolling moment coefficient obtained using the SST model calculations were performed with a coefficient of 10 (Menter's suggested value [57]) and 10000 (the limiter effectively off as the ratio of production to destruction never exceeds this value). The results are presented in Fig. 16. And show that the effect of the limiter is significant, resulting in a rolling moment coefficient for the limited case that is twice that of the unlimited case. This result highlights the sensitivity of the computed flows to the turbulence production. By limiting the turbulence production it is possible to reduce the effective turbulent viscosity which in turn reduces the rate of growth of the vortex leading to stronger vortices downstream. As a consequence subsequent interactions between the vortices and with downstream aerodynamic surfaces are changed.
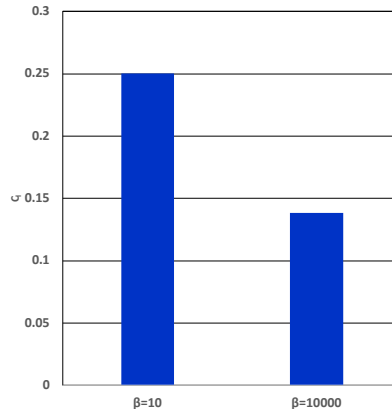

Fig. 16 Comparison of rolling moment coefficients obtained with and without the production term limiter (SST Model, Corvid Technologies, unstructured mesh).

3. Rotational and Curvature Correction

For fully developed trailing vortices generated by aircraft wings, Bradshaw [59] observed that the behavior of the vortex core, in particular it's growth, was generally much more laminar like than would be expected. Although made for mature trailed vortices, his observation appears to apply to a much broader range of vortex flows. This has significant implications for the current flow, which is dominated by interactions between co- and counter-rotating vortices. Indeed, in the case of counter-rotating vortices, the ratio of core size to the distance between cores is an important parameter in determining whether the vortices will continue to orbit one another or begin to undergo viscous merging. The weakness of standard SA and SST models for vortical flows is well known and can be easily related to the fact that the models were primarily developed, and calibrated, for simple shear flows that involve homogenous turbulence and thin shear layers.

In an effort to overcome these limitations, a number of investigators have proposed modifications to the standard models that seek to sensitize the predicted turbulence to the effects of system rotation and streamline curvature.

Shur *et al* [60] follow an approach that is close in concept to ideas originally proposed by Knight and Saffman [61] that tracks the direction of the principal axes. However, the details of their formulation result in an approach that is more readily amenable to implementation in an unstructured three-dimensional finite volume solver. The application of the concepts to the SA turbulence model results in only one key difference, the multiplication of the production term in Equation 4 by a rotation function so that,

$$S_P = c_{b1}(1 - f_{t2})f_{r1}\hat{S}\hat{v} \qquad (4a)$$

The rotation function f_{r1} attempts to account for the effects of both streamline curvature and system rotation. The formulation of this term can be found in [60]. Results from this model will be designated using SA-noft2-RC or SA-neg-RC depending on the underlying formulation of the model.

An alternative approach has been proposed by Dacles-Mariani *et al* [62,63] who attempt to reduce the eddy viscosity in regions where vorticity exceeds strain rate. In regions of pure rotation, such as in the core of a vortex this modification should result in no turbulent production. Elsewhere, for example in simple shear layers, where vorticity and strain are almost equal, the modeled production should revert to that of the original model. The model is identical to the original SA model, except that the magnitude of vorticity in the production term is replaced with,

$$\Omega + C_{rot}min(0, S - \Omega) \qquad (16)$$

Further details can be found in [62,63]. Results from this model will be designated SA-noft2-R or SA-neg-R depending on the underlying formulation of the model.
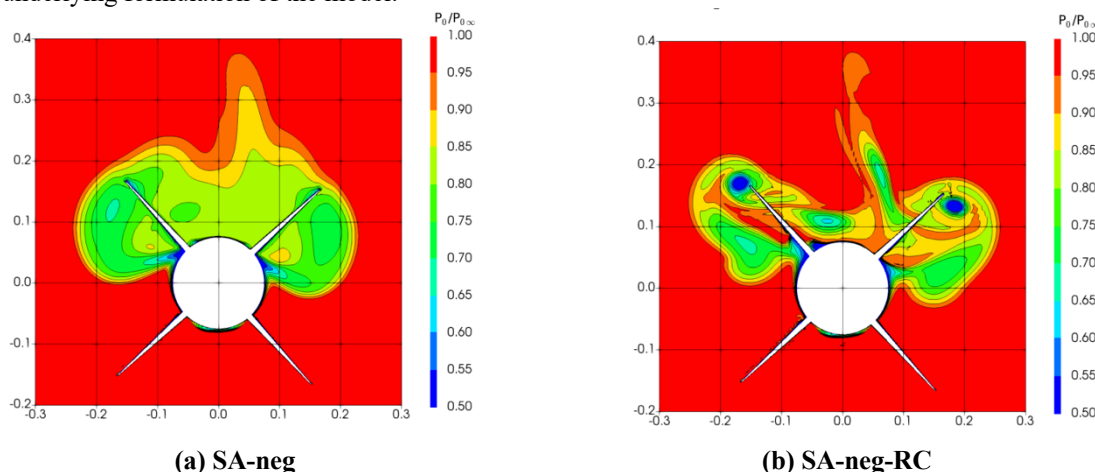

(a) SA-neg   **(b) SA-neg-RC**

Fig. 17 Normalized total pressure Contours, x/D = -21.5 (DLR, unstructured mesh).

(a) SA-noft2   **(b) SA-noft2-RC**
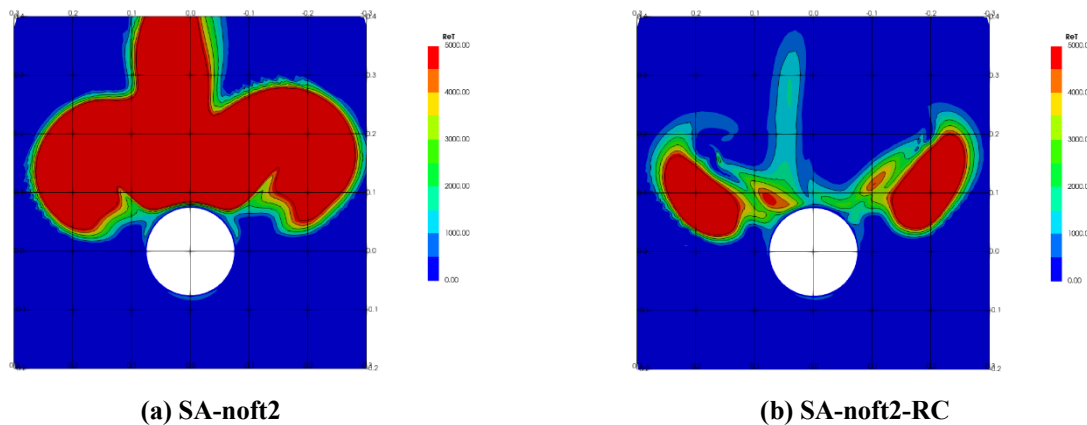
Fig. 18 Turbulent Reynold number contours, x/D = -21.5 (DLR, unstructured mesh).

(a) lateral location of vortex core　**(b) vertical location of vortex core**
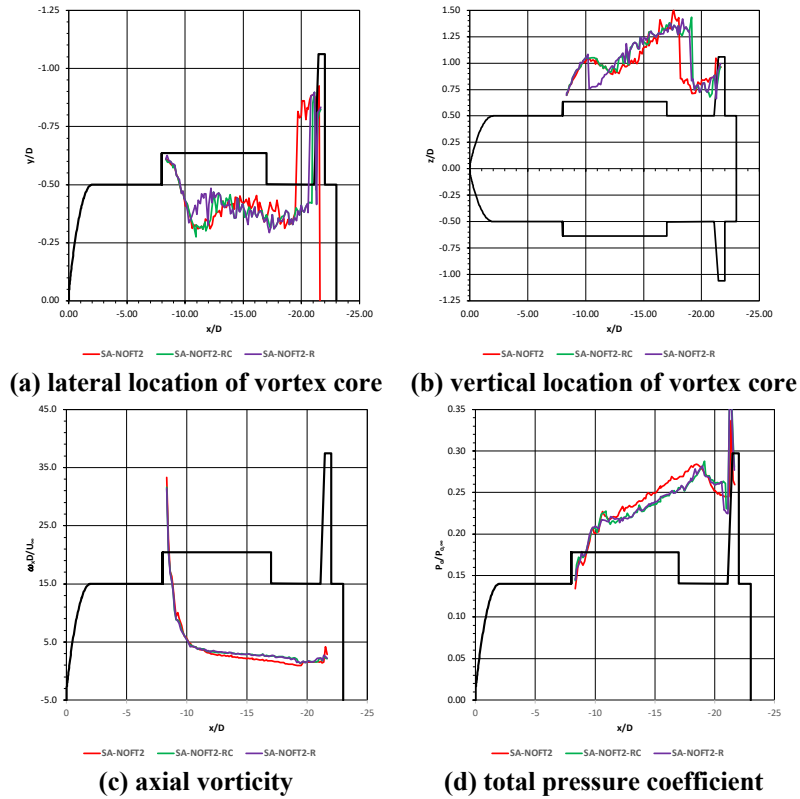

(c) axial vorticity　**(d) total pressure coefficient**

Fig. 19 Effect of rotation correction on leeside vortex descriptors (Corvid Technologies, unstructured mesh).

(a) lateral location of vortex core　**(b) vertical location of vortex core**

(c) axial vorticity　**(d) total pressure coefficient**
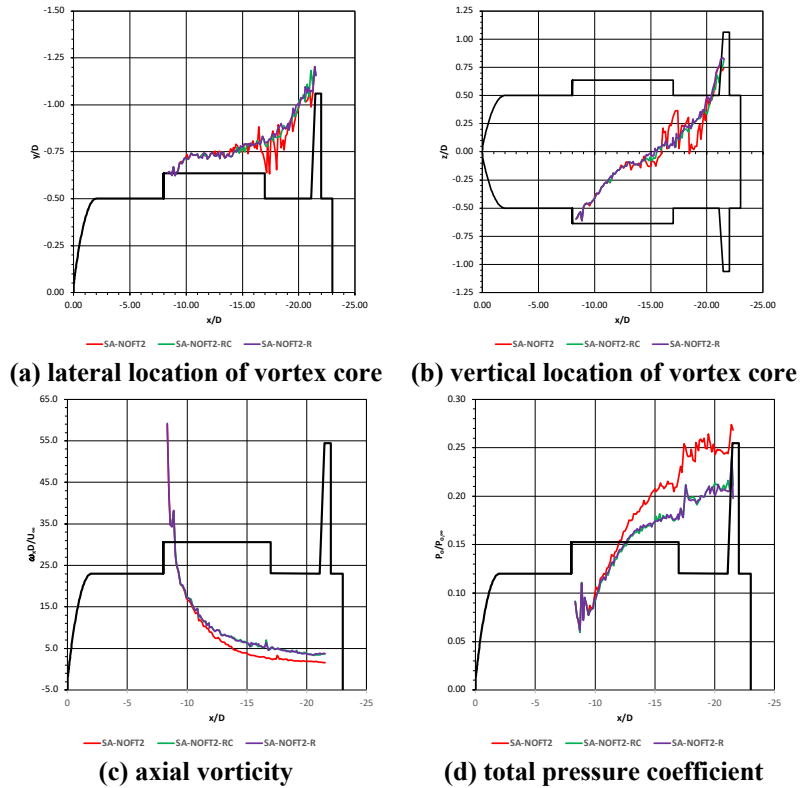
Fig. 20 Effect of rotation correction on windward vortex descriptors (Corvid Technologies, unstructured mesh).

19

Fig. 17 and Fig. 18 presents computed total pressure contours and computed turbulent Reynolds number at x/D = -21.5 computed using the SA-noft2 and SA-noft2-RC models. The rotational correction has a significant impact on the structure of the solution. The vortical structures are stronger and more coherent as are other details, such as the wakes generated by the wings. This is also reflected in the details of the leeside and windward side vortex systems, Fig. 19 and Fig. 20. The trajectories obtain with both the SA-noft2-R and SA-noft2-RC models are much closer to that of the SST model, in particular the leeside lateral location of the vortex core. The intensity of the vortex is much greater compared to the original SA-noft model, indeed the SA-noft-RC model produces results that are close to those of the SST model. These changes are reflected in much larger values of computed rolling moment coefficient, Fig. 21.
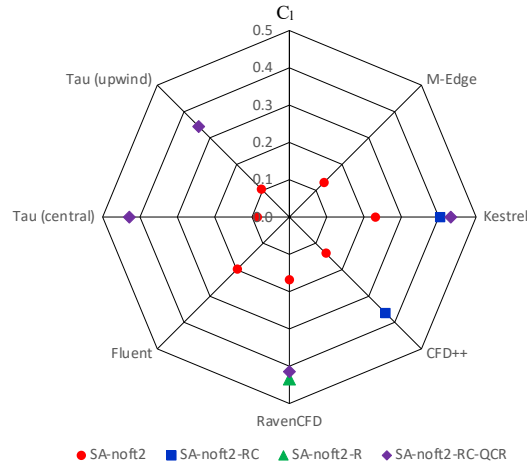

Fig. 21 Influence of rotation correction on computed rolling moment coefficient (unstructured mesh).

The results obtained using the rotation and streamline curvature corrections again illustrates the sensitivity of the results to the production of turbulence. This is most evident in Fig. 18 which shows significant reductions in the effective eddy viscosity throughout the flow. Although the values of eddy viscosity in the vortex regions remains high, they are much lower than without the corrections (the saturation of the contours masks this change in the figure). The resulting reduction in viscous diffusion had a direct, first order, effect on the vortices. They grow more slowly, and consequently downstream interactions between vortices, in particular the convective merging of the lee and windward side vortex systems is affected. This in turn changes the nature of the interaction of the vortices with the fins resulting in substantial changes in the rolling moment experienced by the airframe.
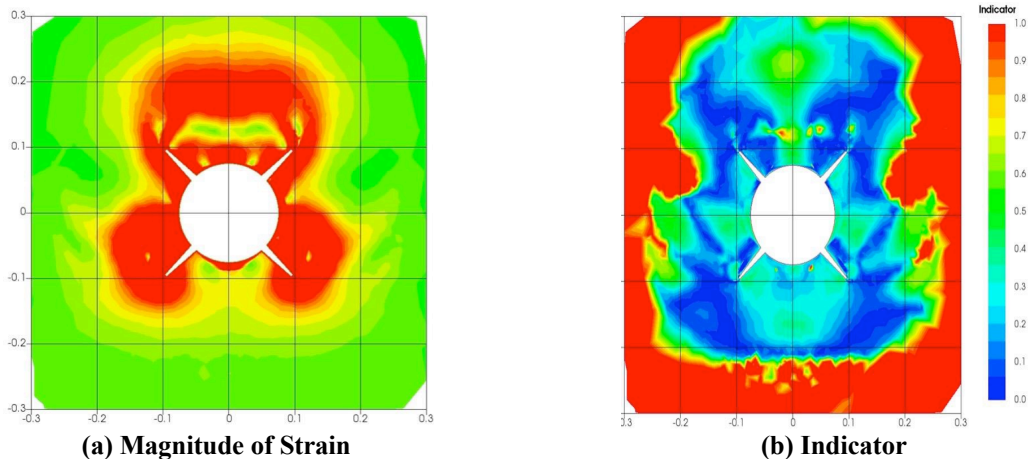

(a) Magnitude of Strain   **(b) Indicator**

Fig. 22 Validity of the Boussinesq hypothesis (x/D = -10.0, MBDA-UK, structured mesh).

4. Non-linear and Reynold stress transport models

The models presented thus far have employ the Boussinesq hypothesis to relate the Reynolds' stresses to the averaged velocity field. In order to test the validity of the hypothesis Schmitt [64] and Schmitt and Hirsch [65] introduced an indicator, ρ, that is analogous to a dot product of two vectors. The results of computations performed using a Reynolds stress transport model are presented in Fig. 22, the figure shows magnitude of strain and Schmitt's indicator at a location 2 calibers aft of the wing leading edge. This result suggests that without significant calibration linear eddy viscosity models may be inadequate to describe the complex, highly strained flow encountered in this work.

To modify the Boussinesq assumption Spalart [66] introduce additional quadratic terms in the relationship between the Reynolds' stresses and the mean flow,

$$\widetilde{\tau_{\iota J}} = \tau_{ij} - 2c_{r1}\mu_t\left(O_{ik}S_{jk} + O_{jk}S_{ik}\right) \tag{17}$$

in which O_{ik} is an antisymmetric normalized rotation tensor (see [66] for full details). Results obtained using this approach will be designated with the suffix -QCR. Computed contours of total pressure at x/D = -23.05are presented in Fig. 23 and Fig. 24 based upon the SA model, Sa-noft2-RC-QCR, and SST models, SST-QCR. While there are some small differences in the flow topology the rolling moment coefficient is not significantly affected, Fig. 25. Indeed the results suggest that the curvature correction is most significant (see also the comparison of total pressure coefficients in Fig. 23). An explanation for this behavior can be seen in Fig. 26, which compares contours of turbulent kinetic energy number at x/D = -23.5 obtained using the SST and SST-QCR models. It can be seen that the QCR modification has little impact on turbulent kinetic energy and, we can infer, the effective turbulent viscosity.
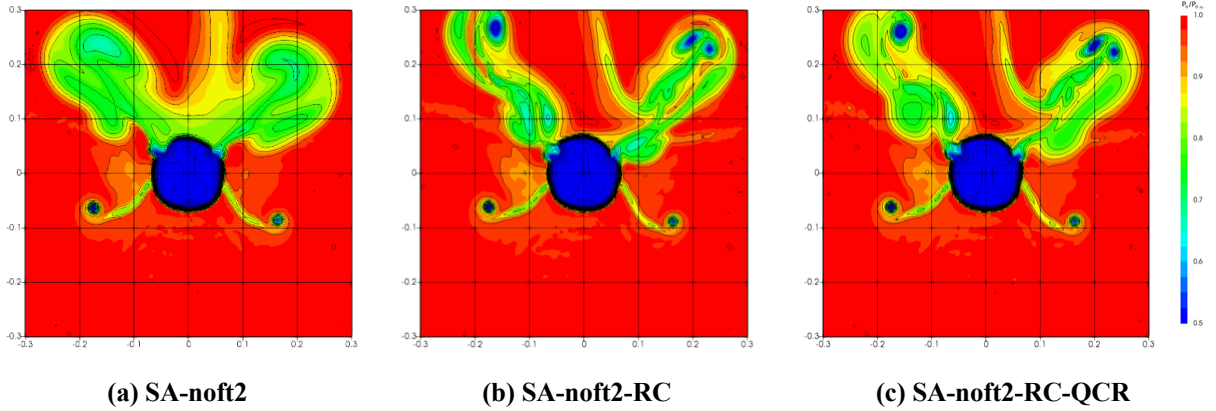

| (a) SA-noft2 | (b) SA-noft2-RC | (c) SA-noft2-RC-QCR |

Fig. 23 Contours of normalized total pressure, x/D = -23.5 (Corvid Technologies, unstructured mesh).
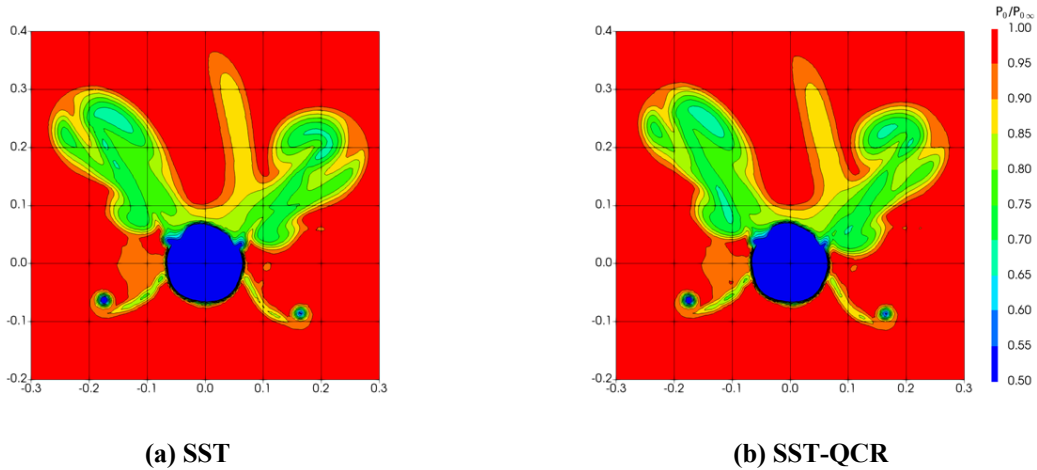

| (a) SST | (b) SST-QCR |

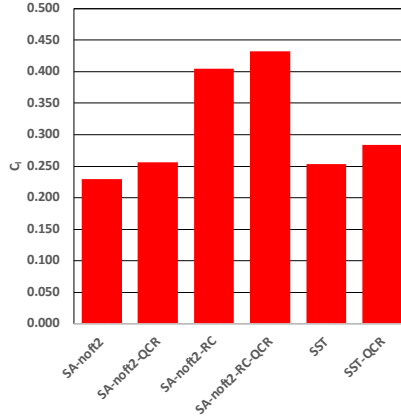**Fig. 24 Contours of normalized total pressure, x/D = -23.5 (ARL, unstructured mesh).**

Fig. 25 Comparison of computed rolling moment coefficient with and without QCR modification (ARL, unstructured mesh).
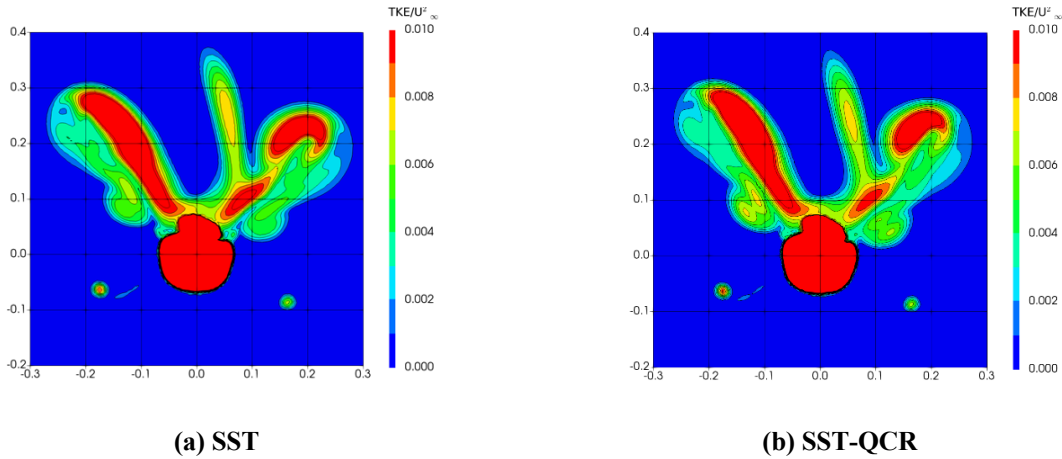

(a) SST	(b) SST-QCR

Fig. 26 Contours of turbulent kinetic energy, x/D = -23.5 (ARL, unstructured mesh).

An algebraic Reynolds stress model (ARSM) can be developed from the Reynolds stress transport equations by assuming that the advection and diffusion of the individual Reynolds stresses can be expressed as a product of the corresponding quantity for the turbulent kinetic energy, k, and the individual Reynolds stresses normalized by k. This assumption allows an implicit relationship between the Reynolds' stresses and the mean velocity to be used in place of the Boussinesq hypothesis. Since the algebraic Reynolds stress model is derived from an RST model many of the characteristics of the underlying model are inherited and the approach represents a systematic approach to dealing with aspects of system rotation and streamline curvature [66]. Unfortunately the ARSM approach is cumbersome to implement and use. Instead Wallin and his co-workers [66] propose the use of an explicit algebraic relationship between the Reynolds' stresses and mean-velocity field, resulting in a non-linear model that is of comparable complexity and cost as conventional two-equation eddy viscosity models. This class of models is referred to as explicit algebraic Reynolds stress models (EARSM).

Fig. 27 and Fig. 28 compare contours of total pressure and turbulent Reynolds number at x/D = -21.5 obtained using an SST (with no production term limiter, i.e. $\beta = \infty$) and EARSM model. The results show large changes in the structure of the flow. The flow field computed using the EARSM model exhibits greater structure, with intense compact vortices, evidence of the convective merging between the leeward and windward vortex systems and wake structures. This detail appears to be related to a reduction in effective eddy viscosity, Fig. 28, which exhibits physically unreasonable behavior in the case of the SST computation. The impact on computed rolling moment coefficient is shown in Fig. 29. The results of the EARSM model show a near doubling in computed rolling moment when compared with the SA-noft2 model, but only a slight increase when compared with the SST results. The apparent inconsistency between the results shown in Fig. 27 – 28 and Fig. 29 may in part be explained by the use of a production term limiter in the latter calculations.
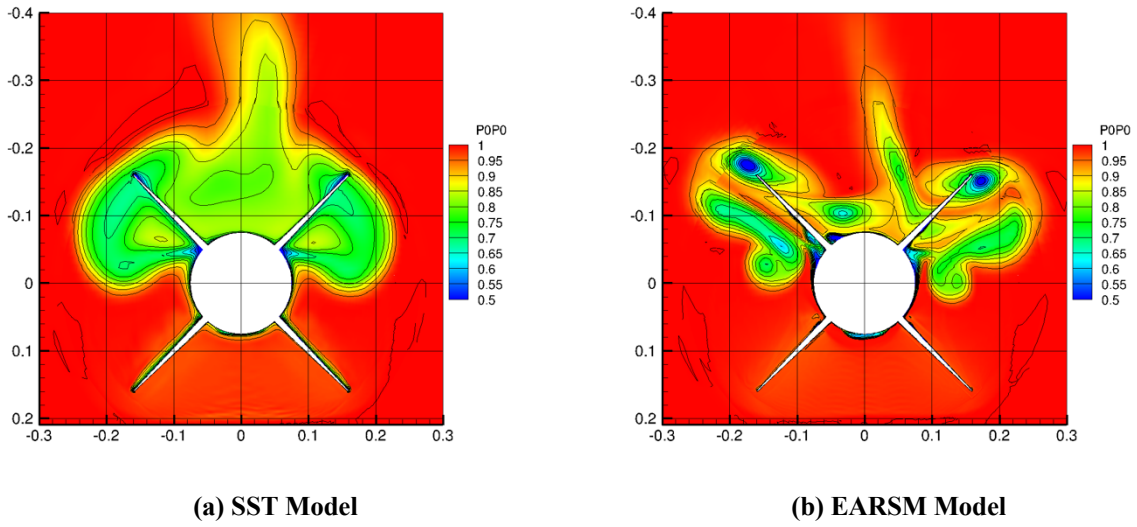
22

(a) SST Model

(b) EARSM Model

Fig. 27 Normalized total pressure contours, x/D = -21.5 (Glasgow University, structured mesh).

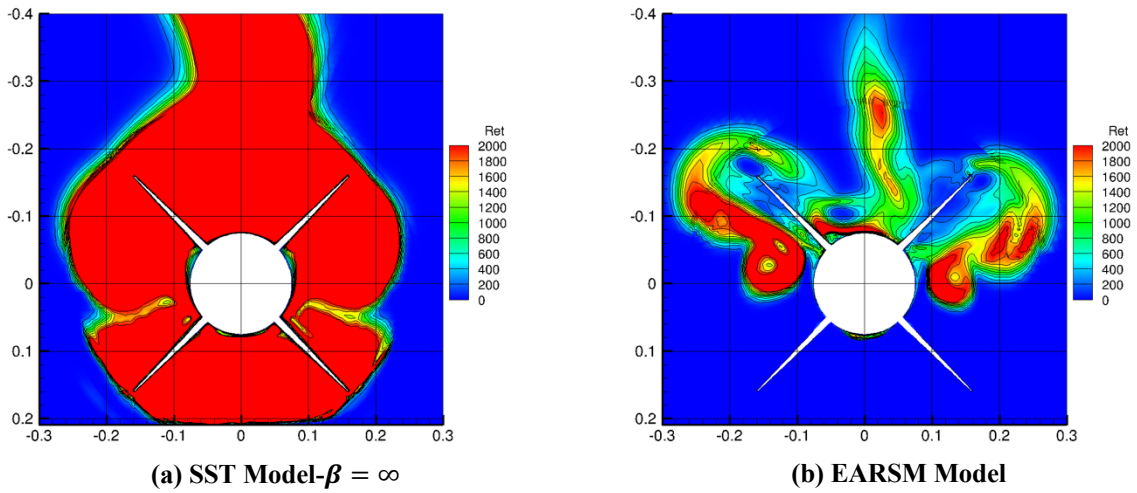

(a) SST Model-$\beta = \infty$

(b) EARSM Model

Fig. 28 Comparison of EARSM and SST-$\beta = \infty$ model predictions of turbulent Reynolds number, x/D = -21.5 (Glasgow University, structured mesh).
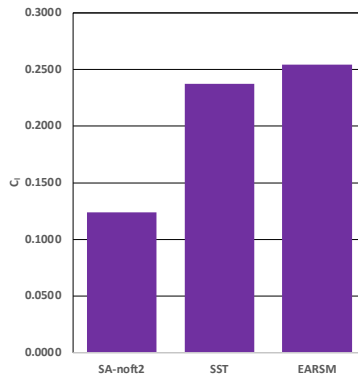

Fig. 29 Comparison of computed rolling moment coefficients (FOI, unstructured mesh).

By taking additional moments of the transport equations for the velocity fluctuations one can derive, see [50] for example, transport equations for the individual Reynolds stresses of the form,

$$\frac{DR_{ij}}{Dt} = D_{ij} + P_{ij} + \Pi_{ij} + \Omega_{ij} - \varepsilon_{ij} \qquad (18)$$

in which the terms on the right-hand side represent diffusion, production, transport due to the correlation between pressure and strain, transport due to rotation and dissipation respectively. The production term is known exactly, but all of the other terms on the right-hand-side must be modeled. The details of the closure are beyond the scope of the present paper, for the results presented below the SSG/LRR-ln(ω) formulation [67] was used. This model will be designated by RSTM.

Computed total pressure contours at $x/D = -21.5$ obtained with the RSTM and SST models are presented in Fig. 30. The vortical flow computed with the RSTM model shows evidence of more intense compact vortices and details of the convective merging between the leeside and windwards side vortex systems exhibit some difference resulting in different vortex trajectories. Changes to the strength and position of the vortices and their interaction with the fins results in large changes to the computed rolling moment coefficient, Fig. 31.
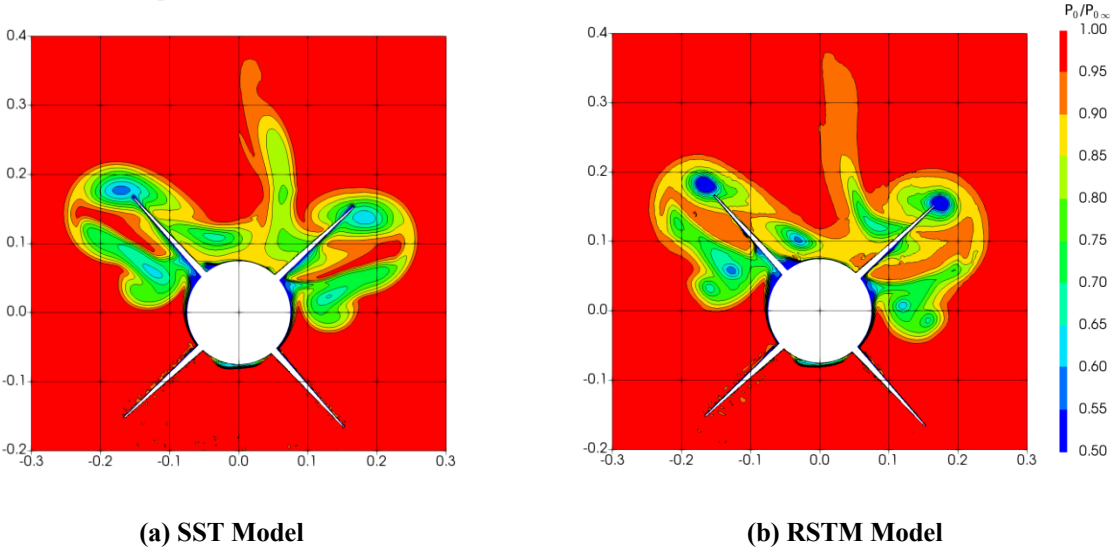

(a) SST Model   **(b) RSTM Model**

Fig. 30 Comparison of SST and RSTM model predictions of contours of normalized total pressure, $x/D = -21.5$ (DLR, unstructured mesh).
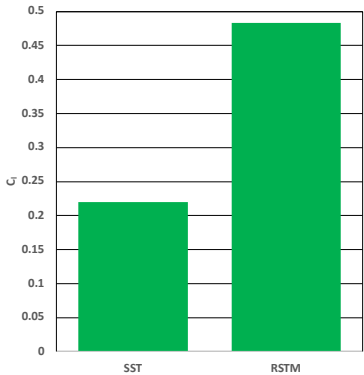

Fig. 31 Comparison of computed rolling moment coefficients (DLR, unstructured mesh).
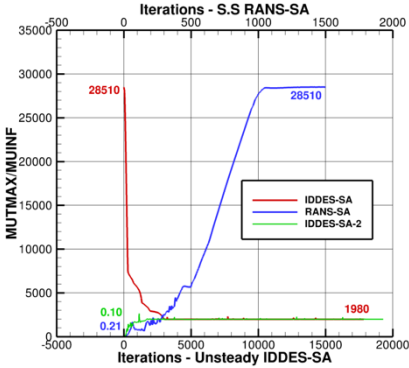
Fig. 32 Iterative convergence of maximum turbulent Reynolds number (ARL, unstructured mesh).

V. Conclusions

Within the framework of the NATO Science and Technology Organization Applied Vehicle Technology Task Group AVT316 calculations have been made of the supersonic flow around a slender body with wings and fins. A synthesis of the results obtained using the Reynolds Averaged Navier-Stokes equations was presented.

The results show significant sensitivity to the choice of turbulence model with values of rolling moment coefficient in the range $0.1 - 0.5$ being obtained. Whilst the gross features of the flow are similar, the detailed development of the leeward wake and the interaction between the leeward and windward vortex systems downstream of the wings show significant differences depending on the model employed.

Simple linear eddy viscosity models predict vortices that rapidly decay, resulting in weak interactions with the downstream fins and relatively small rolling moments. This is attributed to an over production in turbulence quantities that results in excessive effective turbulent viscosity.

Interventions that limit the production of turbulence, for example the SST limiter or curvature corrections, results in vortices that grow more slowly, changing the nature of the downstream interactions resulting in increased rolling moment. The use of more complex formulations, such as Reynolds stress models, that are inherently more capable for highly strained flows, further limits the rate of growth of the vortex cores leading to rolling moment predictions that are 2-5 times greater than those obtained with the simplest models.

The results suggest that standard turbulence models, such as the SA-noft2 and SST model (without production limiter) are not qualified for vortex dominated flows. Interventions that seek to limit turbulence production appear to provide results that are more reasonable, in particular with regard to the amount of effective turbulent viscosity predicted by the models. Although there are no physical measurements to support this statement, the results that have been generated provide a compelling argument for this belief. Comparisons with scale-resolving simulations, which directly resolve the largest turbulent eddies seem to confirm this. Fig. 32 presents iterative convergence histories of the maximum turbulent Reynolds number obtained using the SA-noft2 model and two different scale resolving models and show that the use of a simple turbulence model results in a maximum turbulent Reynolds number an order of magnitude larger compared to that seen in the scale-resolving simulations. The application of scale-resolving approaches to the OTC1 test case is explored more fully in a companion paper [6].

Acknowledgments

References

[1] Taylor, N. et al., "The Prediction of Vortex Interactions on a Generic Missile Configuration Using CFD: Current Status of Activity in NATO AVT-316," NATO STO-MP-AVT-307, Paper 24, October 2019.

[2] Taylor, N., "AVT-316 Missile Facet: Overview of its Formation, Objectives and Manner of Working", paper to be presented at AIAA SciTech 2022, January 2022.

[3] Dikbaş E., et al., "The Influence of the Computational Mesh on the Prediction of Vortex Interactions about a Generic Missile Airframe", paper to be presented at AIAA SciTech 2022, January 2022.

[4] Park, M.A., and DeSpirito, J., "The Influence of Adaptive Mesh Refinement on the Prediction of Vortex Interactions about a Generic Missile Airframe", paper to be presented at AIAA SciTech 2022, January 2022.

[5] Anderson, M et al., "The Influence of the Numerical Scheme in Predictions of Vortex Interaction about a Generic Missile Airframe", paper to be presented at AIAA SciTech 2022, January 2022.

[6] Tormalm, M., et al., "The Influence of Scale Resolving Simulations in Predictions of Vortex Interaction about a Generic Missile Airframe", paper to be presented at AIAA SciTech 2022, January 2022.

[7] Boychev, K., Barakos, G. and Steijl, R., "Simulations of flows around complex and simplified supersonic store geometries at high incidence angles using statistical and scale resolving turbulence models", paper to be presented at AIAA SciTech 2022, January 2022.

[8] Loupy, G.J.M., "A Focused Study into the Prediction of Vortex Formation about Generic Missile and Combat Aircraft Airframes", paper to be presented at AIAA SciTech 2022, January 2022.

[9] Schnepf, C., and Tormalm, M., "Comparisons of predicted and measured aerodynamic characteristics of the DLR LK6E2 missile airframe", paper to be presented at AIAA SciTech 2022, January 2022.

[10] DeSpirito, J., et al., "Comparisons of Predicted and Measured Aerodynamic Characteristics of the DLR LK6E2 Missile Airframe (Scale Resolving)", paper to be presented at AIAA SciTech 2022, January 2022.

[11] Taylor, N., "AVT-316 Missile Facet: 316 Missile Facet: Lessons learned concerning the prediction of Vortex Flow Interactions about Generic Missile Configurations", paper to be presented at AIAA SciTech 2022, January 2022.

[12] Smith, J. H. B., "A review of separation in steady three-dimensional flow," AGARD CP-168, May 1975.

[13] Luckring, J., "The discovery and prediction of vortex flow aerodynamics," The Aeronautical Journal, Vol. 123, No. 1256, June 2019. Pp. 729-804.

[14] Oberkampf, W.L. and Bartel, T.J., "Supersonic Flow Measurements in the Body Vortex Wake of an Ogive Nose Cyclinder," Report No. AFATL-TR-78-127, University of Texas at Austin, Department of Mechanical Engineering, 1978.

[15] Jorgensen L.H. and Perkins, E.W., "Investigation of some wake vortex characteristics of an inclined ogive-cylinder body at Mach No. 2," NACA Report 1371, 1955.

[16] Mello, J.F., "Investigation of normal force distribution and wake vortex characteristics of bodies of revolution at supersonic speeds," Journal of Aerospace Science. Vol. 26, pp. 155-168, March 1959.

[17] Tinling, B.E. and Allen, C.Q., "An investigation of the normal force and wake characteristics of an ogive cylinder," NASA TN D-1297, 1962.

[18] Fiechter, M., "Ueber Wirbelsysteme an Schlanken Rotationskorpern und Ihren Einfluss auf die Aerodynamischen Beiwerte," Report No.: AFATL-TR-78-127, Deutsch-Fraenzosisches Forschungsinstitut; 1966.

[19] Grosche, F.R., "Wind tunnel investigation of the vortex system near an inclined body of revolution with and without wings," AGARD CP-71-71, 1971.

[20] Fidler J.E., Nielsen, J.N. and Schwind, R.G., "An investigation of slender-body wake vortices," AIAA Paper 77-7, January 1977.

[21] Yanta, W.J. and Wardlaw, A.B., "Laser Doppler velocimeter measurements of leeward flowfields on slender bodies at larger angle of attack," AIAA Paper 77-660, 1977.

[22] Owen, F.K., "Wake vortex measurements of bodies at high angle of attack," AIAA Paper 78-23, January 1978.

[23] Khalid, M., Essers, J.A,, Bredif, M., Kunetzmann, P., Lacau, R. and Dujardin, A., "Assessment of turbulence modeling for high-speed vehicles,", Report No. TR-AVT-082, NATO RTO, 2005.

[24] Amato, M., van den Berg, J.I., Systma, H.A. and Prananta, B.B.. "GARTEUR-AG24, Missile Aerodynamics: Navier-Stokes calculations of supersonic flow about slender configurations - Results of circular ogive cylinder configuration (B1 Test Case)," GARTEUR Report No. TP-109-1, 2003.

[25] Champigny, P., "GARTEUR-AG24, Missile Aerodynamics: Navier-Stokes calculations of supersonic flow about slender configurations Synthesis Report," GARTEUR Report No. TP-109-4, 2003.

[26] Wrisdale, I.E,, Birch, T.J. and Prince, S.A., "GARTEUR-AG24, Missile Aerodynamics: Navier-Stokes calculations of supersonic flow about slender configurations Comparison of computational and experimental results for a body-wing configuration at Mach 2.5," GARTEUER Report No. TP-109-3, 2003.

[27] Champigny, P., "GARTEUR-AG24, Missile Aerodynamics: Navier-Stokes calculations of supersonic flow about slender configurations, Comparison of computational and experimental results for a body of revolution at Mach 2 in turbulent flow (Test Case B2)," GARTEUR Report No. TP-109-2, 2003.

[28] Birch, T.J., Wrisdale, I.E., Prince, S.A., "CFD predictions of missile flowfields," AIAA Paper 2000-4211, 2000.

[29] Sturek, W.B., "KTA-12: Application of CFD to the prediction of missile body vortices," TTCP Report No. KTA-12 Final Report, 1997.

[30] Saffman, P.G., *Vortex dynamics,* Cambridge University Press, Cambridge, England, UK, 1993.

[31] Govindaraju, S. P. and Saffman, P. G., "Flow in a turbulent trailing vortex," Physics of Fluids, vol. 14, no. 10, pp. 2074-80, October 1971.

[32] Zeman, O., "The persistence of trailing vortices: A modelling study," Physics of Fluids, vol. 7, no. 1, pp. 135-143, January 1995.

[33] Spalart, P. and Garbaruk, A., 'The predictions of common turbulence models in a mature vortex', Flow Turbulence and Combustion, Vol. 102:667-77, 2018.

[34] Doligalski, T.L., Smith, C.R., and Walker, J.D.A., 'Vortex interactions with walls', Annual Review of Fluid Mechanics, Vol. 26:573-616, 1994.

[35] Dee, F.S. and Nicholas, O.P., 'Flight measurements of wing-tip vortex motion near the ground', Aeronautical Research Council CP 1065, 1968.

[36] Harvey, J.K. and Perry, F.J., 'Flowfield produced by trailing vortices in the vicinity of the ground', AIAA J., Vol 9:1659-60, 1971.

[37] Shabaka, I. M. M. A., Mehta, R. D. and Bradshaw, P., 'Longitudinal vortices imbedded in turbulent boundary layers. Part 1. Single vortex', Journal of Fluid Mechanics, Vol. 155:37–57, 1985.

[38] Mehta, R. D. and Bradshaw, P., 'Longitudinal vortices imbedded in turbulent boundary layers, part 2. vortex pair with 'common flow' upwards', Journal of Fluid Mechanics Vol. 188:529–546, 1988.

[39] Lin, J. C., 'Review of research on low-profile vortex generators to control boundary-layer separation', Progress in Aerospace Sciences, Vol. 38:389–420, 2002.

[40] Peace, A.J., and Riley, N. A., 'Viscous vortex pair in ground effect', J. Fluid Mech., Vol. 129:409, 1983.

[41] Spalart, P.R., Strelets, M. Kh., Travin, A.K. and Shur, M.L., 'Modelling the interaction of a vortex pair with the ground', J. Fluid Dynamics, Vol. 36:899-908, 2001.

[42] Allan, B.G., Chung-Sheng, Y., and Lin, J.C., 'Numerical simulations of vortex generator vanes and jets on a flat plate', AIAA-Paper-2002-3160, 2002.

[43] Wik, E., and Shaw, S.T., 'Numerical simulation of micro vortex generators', AIAA-Paper 2004-2697, 2004.

[44] Cutler, A.D. and Bradshaw, P., 'Strong vortex/boundary layer interactions: Part I. Vortices high', Experiments in Fluids, Vol. 14:321-332, 1993.

[45] Cutler, A.D. and Bradshaw, P., 'Strong vortex/boundary layer interactions: Part II. Vortices low', Experiments in Fluids, Vol. 14:393-401, 1993.

[46] Meunier, P., Le Dizès, S. and Leweke, T., "Physics of vortex merging," Comptes Rendus Physique, Centre Mersenne, Vol. 6, No. 4-5, pp.431-450, 2005.

[47] Spalart, P.R., Allmaras, S.R.,. "A One-Equation Turbulence Model For Aerodynamic Flows," AIAA Paper 92-0439, January 1992.

[48] Menter, F.R., "Two-Equation Eddy-Viscosity Turbulence Models for Engineering Applications", AIAA Journal Vol. 32 No. 8, pp. 1598-1605, August 1994.

[49] White, F. Viscous Fluid Flow, 3rd ed., McGraw-Hill; 2006.

[50] Wilcox, D., Turbulence Modeling for CFD, DCW Industries, 1998.

[51] Spalart, P., "Detached Eddy Simulation", Annual Review of Fluid Mechanics, Vol. 41., pp. 181-202, January 2009.

[52] AIAA Turbulence Model Benchmarking Working Group, Turbulence Modeling Resource, https://turbmodels.larc.nasa.gov/index.html.

[53] Allmaras, S.R., Johnson, F.T. and Spalart, P.R., "Modifications and Clarification for the Implenetation of the Spalart-Allmaras Turbulence Model," ICCFD Paper 7-1902, 2012.

[54] Mendenhall, M.R. and Nielsen, J.N., "Effect of symmetrical vortex shedding on the longitudinal characteristics of wing-body-tail combinations," NASA CR-2473, 1975.

[55] Wilcox, D.C., "Formulation of the k-omega Turbulence Model Revisited," AIAA Journal, Vol. 46 No. 11, pp. 2823-2838, November 2008.

[56] Jones, W.P. and Launder, B.L., "The prediction of laminarization with a two-equation model of turbulence," International Journal of Heat and Mass Transfer, Vol. 15. 1972.

[57] Menter, F.R., "Zonal Two Equation k-omega Turbulence Models for Aerodynamic Flows," AIAA Paper 93-2906, 1993.

[58] Menter, F. R., Kuntz, M., and Langtry, R., "Ten Years of Industrial Experience with the SST Turbulence Model," Turbulence, Heat and Mass Transfer 4, pp. 625 - 632, 2003.

[59] Bradshaw, P. "Effects of streamline curvature on turbulent flow," AGARDograph 169, 1973.

[60] Shur, M. L., Strelets, M. K., Travin, A. K., Spalart, P. R., "Turbulence Modeling in Rotating and Curved Channels: Assessing the Spalart-Shur Correction," AIAA Journal Vol. 38, No. 5, pp. 784-792, 2000.

[61] Knight, D. D., and Saffman, P. C., "Turbulence Model Predictions for Flows with Significant Mean Streamline Curvature," AIAA Paper 78-258, 1978.

[62] Dacles-Mariani, J., Zilliac, G. G., Chow, J. S., and Bradshaw, P., "Numerical/Experimental Study of a Wingtip Vortex in the Near Field," AIAA Journal, Vol. 33, No. 9, pp. 1561-1568, 1995.

[63] Dacles-Mariani, J., Kwak, D., and Zilliac, G. G., "On Numerical Errors and Turbulence Modeling in Tip Vortex Flow Prediction," Int. J. for Numerical Methods in Fluids, Vol. 30, pp. 65-82, 1999.

[64] Schmitt, F.G., "About Boussinesq's turbulent viscosity hypothesis: historical remarks and a direct evaluation of its validity," Comptes Rendus Mécanique, Vol. 335, Issues 9–10, pp. 617-627, September–October 2007.

[65] Schmitt, F.G. and Hirsch, C., "Direct test of Boussinesq's hypothesis and the k-transport equation using experimental, DNS and LES data," Proceedings of the 5th International Symposium on Engineering Turbulence Modelling and Measurements, Mallorca, Spain, pp. 167-176, 16–18 September, 2002.

[66] Wallin, S. and Johansson, A., "An Explicit Algebraic Reynolds Stress Model for Incompressible and Compressible Turbulent Flows," Journal of Fluid Mechanics, Vol. 403, pp. 89-132, 2000.

[67] Cecora, R.-D., Radespiel, R., Eisfeld, B., and Probst, A., "Differential Reynolds-Stress Modeling for Aeronautics," AIAA Journal, Vol. 53, No. 3, pp. 739-755, 2015.

[68] Luckring, J. et al, "AVT-316: Vortex Interaction Effects Relevant to Military Air Vehicle Performance," NATO STO-TR-AVT-316, to be published in 2022.